Targeting sterol regulatory element binding proteins (SREBPs) activation lowers intraocular pressure by halting its mechanosensing function in the trabecular meshwork

Ting Wang[1,2], Avinash Soundararajan[1], Jeffery Rabinowitz[3], Anant Jaiswal[4], Timothy Osborne[4], Padmanabhan Pattabiraman[1,2]

[1]Glick Eye Institute, Department of Ophthalmology, Indiana University School of Medicine, 1160 West Michigan Street, Indianapolis, Indiana, 46202, United States of America

[2]Stark Neuroscience Research Institute, 320 W. 15th Street, Indiana University School of Medicine, Indiana, 46202, United States of America

[3]Departments of Ophthalmology, Case Western Reserve University, Cleveland, Ohio , United States of America

[4]Institute for Fundamental Biomedical Research, Departments of Medicine and Biological Chemistry, Johns Hopkins University School of Medicine, St. Petersburg, Florida, 33701, United States of America

Key Words: Intraocular pressure, trabecular meshwork, sterol regulatory element binding protein, lipid biogenesis, actin cytoskeleton, extracellular matrix

Significance

Elevated intraocular pressure (IOP) is a major risk factor for glaucoma, which is an optic neuropathy and a leading cause of irreversible blindness. Targeting trabecular meshwork (TM) outflow pathway tissue is a significant modality to lower the IOP. The contractile properties of TM tissue play an important role in the regulation of IOP. Though lipids are known to contribute to TM contractility and IOP regulation, the contributions of the lipogenic pathway are not clear. In this study, we identify the mechanosensing role of the lipogenic transcription factors sterol regulatory element binding proteins (SREBPs) in TM. Further, we show that pharmacological or molecular inactivation of SREBPs can lower IOP by modifying actin contractility and ECM remodeling. Thus signifying a novel relationship between SREBP activation status and achieving IOP homeostasis.

Abstract

Trabecular meshwork (TM) cells are highly contractile and mechanosensitive to aid in maintaining intraocular pressure (IOP) homeostasis. Lipids are attributed to modulating the TM contractility with poor mechanistic understanding. In this study using human TM cells, we identify the mechanosensing role of the transcription factors sterol regulatory element binding proteins (SREBPs) involved in lipogenesis. By constitutively activating SREBPs and pharmacologically inactivating SREBPs, we have mechanistically deciphered the attributes of SREBPs in regulating the contractile properties of TM. The pharmacological inhibition of SREBPs by fatostatin and molecular inactivation of SREBPs *ex vivo* and *in vivo* respectively results in significant IOP lowering. As a proof of concept, fatostatin significantly decreased the SREBPs responsive genes and enzymes involved in lipogenic pathways as well as the levels of the phospholipid, cholesterol, and triglyceride. Further, we show that fatostatin mitigated actin polymerization machinery and stabilization, and decreased ECM synthesis and secretion. We thus postulate that lowering lipogenesis in the TM outflow pathway can hold key to lowering IOP by modifying the TM biomechanics.

1. Introduction:

Chronic and sustained elevation in intraocular pressure (IOP) is a significant risk factor for primary open angle glaucoma (POAG) (1-3). A rise in IOP above normal causes mechanical stress and reduced blood flow to the optic nerve(4). This increases the risk of glaucoma with significant consequences on vision and quality of life (5-7). Glaucoma is a major public health concern and the second leading cause of irreversible blindness worldwide afflicting mainly the aging population (8, 9). The estimated number of glaucoma patients in the world is around 80 million with over 2 million in the United States alone (10, 11). Interestingly lowering IOP is neuroprotective and the most effective way to delay the onset of POAG and to halt the progression towards vision loss (12-14). A 20% decrease in IOP significantly alleviates the risk of developing glaucoma (15). The IOP is maintained by the balance between the generation of AH via the ciliary body and drainage mainly via the conventional outflow pathway, which includes trabecular meshwork (TM), juxtacanalicular TM tissue (JCT), and Schlemm's canal (SC) (16). The TM contains an extracellular matrix (ECM) organized into a network of beams lined by highly contractile and mechanosensitive TM cells sensing pressure changes (17-19). Increased actin contractility in TM and ECM hyperdeposition in TM outflow pathway augment AH outflow resistance and IOP elevation (20-22). In POAG, the increased IOP is directly correlated with the increased outflow resistance, and the most characteristic structural change in TM is increased tissue stiffness including ECM accumulation, increased cell contractility, and cell-ECM connections (18, 23-25).

Cellular lipids play important roles in tissue biomechanics by modulating the plasma membrane remodeling, signal transduction cascades, and actin cytoskeleton-cell adhesions linked to the ECM (26). Moreover various lipids found in TM and AH are known to impact IOP homeostasis (27-29). This is attributed via modulating the signaling events including altering the TM contractility and tissue stiffness. Hyperlipidemia is associated with an increased risk of elevated IOP and glaucoma with poor mechanistic understanding (30-32). Interestingly, cholesterol-lowering statins lower IOP and reduce the incidence of glaucoma (33-36). Mechanistic studies in TM point at statin-mediated disruption of membrane association of Rho GTPase due to inhibition of the isoprenylation of Rho (36, 37). We recently found that cyclic mechanical stretch, which mimics mechanical stress on TM, significantly altered lipid contents and increased the expression of cholestogenic enzymes like squalene synthase, 3-hydroxy-3-methylglutaryl coenzyme A (HMG-CoA) synthase (HMGCS) and the transcriptional regulator of lipid biogenesis sterol regulatory element binding protein 2 (SREBP2) in human TM (HTM) cells (38). The SREBPs are master regulator of cellular lipogenesis and occur as three isoforms – SREBP1a, SREBP1c, and SREBP2 (39-41). SREBP1a is involved in overall lipid biosynthesis, SREBP1c regulates fatty acid synthesis, whereas SREBP2 modulates sterol biosynthesis specifically (39-42). SREBPs are basic-helix-loop-helix leucine zipper (bHLH-LZ) transcription factors. Each SREBP precursor has three domains: (1) an NH2-terminal domain including transactivation domain, which is rich in serine and proline and the bHLH-LZ region for DNA binding and dimerization; (2) two hydrophobic transmembrane spanning segments; (3) a COOH-terminal domain (43, 44). Within the cell, following SREBPs mRNA translation, the proform SREBPs (Pro-SREBPs) are bound to SREBP cleavage activating protein (SCAP) forming a SREBP-SCAP complex located on the ER membrane. Stimuli including low lipids levels promote SCAP to guide the whole complex to leave the ER membrane to the Golgi membrane. In the Golgi, the SREBP-SCAP complex is cleaved by site 1 protease (S1P) and site 2 protease (S2P), releasing SCAP from the complex and releasing the active or nuclear SREBPs (N-SREBPs) from Golgi to translocate into the nucleus. Inside the nucleus, N-SREBPs bind to the sterol response element (SRE) on the promoter region of the responsive genes and promote their transcription. These target genes are involved in the fatty acid, triglycerides, and cholesterol biosynthetic pathways by modulating the expression of rate limiting enzymes like acetyl-CoA carboxylase (ACC), fatty acid synthase, and 3-hydroxy-3-methylglutaryl coenzyme A (HMG-CoA)

90 reductase (HMGCR) (42, 44-47). Interestingly, it was earlier reported that there is an isoprenylation of
91 RhoA-dependent and cholesterol-independent actin cytoskeleton contraction, which prevents SREBP1
92 dependent lipogenesis in human immortalized cancer lines and *Drosophila* (48). Such regulatory
93 mechanistic evaluation of lipogenic pathways in AH outflow tract and the role of SREBPs in TM biology
94 lacks understanding. By regulating lipid biogenesis in TM, we believe that SREBPs activities play a
95 significant role in defining actin polymerization and ECM remodeling (49-52). Investigating the
96 mechanosensing function via SREBPs activation paradigm in TM can elucidate how TM cells actively
97 sense and transduce mechanical signals via SREBPs. Thus, we report the biological relevance of SREBPs
98 activation in TM for active pressure sensing to convert mechanical stimuli into TM contractility and
99 mechanistically decipher how the inactivation of SREBPs in the TM outflow pathway lowers IOP.

100 **2. Material and Methods:**

101 **2.1 Materials:**

102 The reagents and antibodies used in this study are documented in Table 1.

103 **TABLE 1:**

Reagents and antibodies	Catalog number	Company
Vinculin	V9131	R&D system
β-actin	A1798	R&D system
Collagen 1α (COL1A)	ab34710	R&D system
LIMK1	sc515585	Santa Cruz Biotechnology
SREBP1	sc13551	Santa Cruz Biotechnology
SREBP2	sc13552	Santa Cruz Biotechnology
Paxillin	sc365379	Santa Cruz Biotechnology
GAPDH	sc32233	Santa Cruz Biotechnology
FAS	sc-48357	Santa Cruz Biotechnology
Fascin 1	sc46675	Santa Cruz Biotechnology
SREBP1	NB100-2215	NOVUS Biologicals
SREBP2	NBP1-54446	NOVUS Biologicals
SREBP2	LS-B1609-BCD1-1	Life Span Bioscience
SCAP	12266-1-AP	Proteintech
SCAP	MABS2288	Sigma-Aldrich
Collagen 1α (COL1A)	ABT257	Sigma-Aldrich
HMGCR	PA5-37367	Invitrogen/ThermoFisher
Lamin B1	PA5-19468	Invitrogen/ThermoFisher
Total-paxillin (T-paxillin)	2542S	Cell Signaling Technology
Phospho-paxillin (P-paxillin)	69363S	Cell Signaling Technology
Total-cofilin (T-cofilin)	5175S	Cell Signaling Technology
Phospho-cofilin (P-cofilin)	3311S	Cell Signaling Technology
ACC	3662S	Cell Signaling Technology
Fibronectin		Gift from Dr. Harold Erickson, Duke University
Donkey-anti-goat IgG	705-035-003	Jackson ImmunoResearch
Donkey-anti-mouse IgG	715-035-150	Jackson ImmunoResearch
Donkey-anti-rabbit IgG	715-035-144	Jackson ImmunoResearch

Goat-anti-Mouse IgG Alexa Fluro Plus 488	A32723	ThermoFisher
Goat-anti-Mouse IgG Alexa Fluor Plus 594	A32742	ThermoFisher
Goat-anti-Rabbit IgG Alexa Fluor Plus 488	A32731	ThermoFisher
Goat-anti-Rabbit IgG Alexa Fluor Plus 594		ThermoFisher
Phalloidin (Alexa Fluor Plus 488 PHA)	A12379	Invitrogen/ThermoFisher
Phalloidin (Alexa Fluor Plus 647 PHA)	A22287	Invitrogen/ThermoFisher
DAPI	UH2820551	Sigma-Aldrich
Fluoromount-G	E139999	Invitrogen/ThermoFisher
Fatostatin	341329	Sigma-Aldrich

104

105 **2.2 Primary TM cell culture:**

106 Primary human TM (HTM) cells were cultured from TM tissue isolated from the leftover donor corneal
107 rings after they had been used for corneal transplantation at the Indiana University Clinical Service,
108 Indianapolis, and characterized as described previously (20, 53). HIPPA compliance guidelines were
109 adhered for the use of human tissues. The usage of donor tissues was exempt from the DHHS regulation
110 and the IRB protocol (1911117637), approved by the Indiana University School of Medicine IRB review
111 board.

112 Primary porcine TM (PTM) cells were cultured from fresh porcine TM globes obtained from Indiana
113 Packers, Delphi, In, USA, as described previously (20).

114 All experiments were conducted using confluent HTM or PTM cultures as mentioned, using cells in
115 between passage four to six, and were performed after overnight serum starvation unless mentioned,
116 otherwise. All experiments in this manuscript were performed using biological replicates.

117 **2.3 Construction of replication-deficient recombinant adenovirus expressing N-SREBPs**

118 Generation of replication-defective recombinant adenovirus expressing N-SREBPs under CMV promoter
119 was performed using ViraPower Adenoviral Expression System (#K4930-00, Invitrogen) as described
120 earlier (54). N-SREBP1a (1470 bps) , N-SREBP1c (1398 bps), and N-SREBP2 (1440 bps) were amplified
121 using high-fidelity PCR (Advantage-HF 2 PCR kit, #639123; Clontech) from human pcDNA3.1-2xFLAG-
122 SREBP1a (#26801, Addgene), pcDNA3.1-2xFLAG-SREBP1c (#26802, Addgene) and pcDNA3.1-2xFLAG-
123 SREBP-2 (#26807, Addgene). Amplified N-SREBP1a (Ad5-N-SREBP1a), N-SREBP1c (Ad5-N-SREBP1c), and
124 N-SREBP2 (Ad5-N-SREBP2) were purified and titres determined.

125 **2.4 Adenovirus-mediated gene transduction in HTM cells**

126 Primary HTM cells were grown on gelatin-coated glass coverslips or in plastic Petri dishes and were
127 infected with Ad5-N-SREBP1a, Ad5-N-SREBP1c, and Ad5-N-SREBP2 or a control empty virus (AdMT) at 50
128 multiplicities of infection for 24 h followed by 48 h serum starvation. Cells were then washed with 1X

129 PBS and were fixed for immunofluorescence (IF) analysis and collected using either TRIZOL for RNA
130 extraction or 1X RIPA for protein extraction.

131 **2.5 Optimization fatostatin for *in vitro* dosing**

132 Fatostatin directly binds to SCAP and inhibits the SREBP-escorting function of SCAP, thereby restricting
133 the translocation of SREBPs from ER to the Golgi and subsequently causing SREBPs inactivation and
134 reducing lipogenesis and fat accumulation (55-57). Overnight serum starvation (~16 h) was carried out
135 on PTM and HTM cultures before treatments. To identify the optimal concentration of fatostatin for
136 lowering SREBPs activation, PTM cells were subjected to 0.2, 2, and 20 µM fatostatin reconstituted in
137 serum-free DMEM for 24 h respectively. Post-treatment, PTM cells were either used for cell viability
138 assay or protein collected for total and nuclear fraction. HTM cells were subjected to the optimal
139 concentration of fatostatin and post-treatment, cells were collected in TRIZOL for RNA isolation or in 1X
140 radioimmunoprecipitation assay (RIPA) buffer for protein isolation along with the cell culture media and
141 stored in -80 °C until used.

142 **2.6 Cell viability assay**

143 The cell viability assay was performed using fluorescein diacetate (FDA) and propidium iodide (PI)
144 staining. PTM cells were grown in 6-well plates until they attained 90% confluency. The cells were
145 treated with a final concentration of 20 µM fatostatin for 24 h followed by overnight serum starvation.
146 FDA-PI double staining was performed based on a previously published protocol with minor
147 modifications (58).

148 **2.7 Cyclic mechanical Stretch:**

149 HTM cells were subjected to cyclic mechanical stretch as published earlier (38). 2 h post stretch, cells
150 were fixed and processed for IF analysis.

151 **2.8 Porcine *ex vivo* elevated IOP model**

152 Elevated IOP was modeled using porcine *ex vivo* perfusion system as described earlier (20, 54). Post
153 perfusion the TM tissue was carefully isolated and frozen at -80°C until further processing.

154 **2.9 *Ex vivo* porcine anterior segment perfusion culture to assess the effect of SREBPs inactivation on**
155 **IOP**

156 The effect of pharmacological SREBPs inactivation on IOP regulation was studied using *ex vivo* porcine
157 anterior segment perfusion culture as described earlier (20). After achieving a stable baseline IOP, the
158 IOP was continuously recorded in the control eyes that received a sham DMSO treatment, and the
159 experimental eyes received 20 µM fatostatin for up to 30h. The changes in IOP (ΔIOP) were calculated as
160 the change in pressure relative to the baseline of drug/sham perfusion. At the end of the perfusion
161 studies, TM tissues were either sectioned for histology studies and fixed with 4% paraformaldehyde, or
162 the TM was collected for protein analysis.

163 **2.10 SCAP-Floxed (*SCAP*$^{f/f}$) mice**

164 All experiments were performed in compliance with the Association for Research in Vision and
165 Ophthalmology (ARVO) Statement for the Use of Animals in Ophthalmic and Vision Research. Mice
166 carrying the floxed Scap allele (B6;129-*Scap*^{tm1Mbjg}/*J*) (59) were obtained from Dr. Tim Osborne, bred,

167 and housed under a standard 12 h light and dark cycle with food and water provided *ad libitum* in the
168 laboratory animal resource center (LARC). Exon 1 of the SCAP gene is flanked with LoxP sites, which are
169 targets for bacteriophage P1 Cre recombinase originally made by Dr. Horton, UTSW Med Center, Dallas
170 (59, 60). They are viable, fertile, normal in size, and do not display any physical or behavioral
171 abnormalities. The genotype was identified by PCR analysis of tail biopsies. All animal procedures were
172 approved by the Institutional Animal Care and Use Committee at the Indiana University School of
173 Medicine and conducted following the Declaration of Helsinki.

174 **2.11 Molecular inactivation of SREBPs *in vivo* in *SCAP$^{f/f}$* mice**

175 Molecular inactivation of SREBPs was achieved by knocking down SCAP in *SCAP$^{f/f}$* mice via intravitreal
176 injection of adenovirus expressing Cre [Ad5.CMV.iCre-eGFP] ($1.6x10^{11}$ pfu/ml). The Ad5.CMV.eGFP
177 ($2.6x10^{11}$ pfu/ml) was used as an adenovirus control and saline injection was used for injection control.
178 These adenoviruses were purchased from the Vector Development Lab, Baylor College of Medicine. Four
179 groups were included in the study: untouched, saline injection, Ad5.CMV.eGFP injection, and
180 Ad5.CMV.Cre-eGFP injection. A 33-gauge needle with a glass microsyringe (10 µL volume; Hamilton
181 Company) was used for the intravitreal injection. Intravitreal injections were performed only in the left
182 eye under a surgical microscope (Trinocular Stereo Zoom Microscope, AmScope). The needle was
183 inserted through the equatorial sclera into the vitreous chamber at an angle of ~ 45°, carefully avoiding
184 contact with the posterior lens capsule or the retina. The right eyes in all groups were left untouched.
185 Viral vectors or saline in a volume of 2 µL were slowly injected into the vitreous over the course of 30
186 seconds. The needle was then left in place for an additional 45 s to avoid leakage before being
187 withdrawn. Before and during intravitreal injection, mice were anesthetized with isoflurane (2.5%)
188 (#NDC 46066-755-04, Patterson Veterinary, Loveland, CO, USA) and 100% oxygen using SomnoSuite
189 (Kent Scientific Corporation, Torrington, CT, USA). Initially, a total of 15 animals/group were used, but
190 post-injection due to infection, cataract formation, and death the final numbers were reduced to 9-10
191 mice/group for the data acquisition with roughly equal number of adult (10-14 months) and old (18-24
192 months) mice.

193 **2.12 Measurement of IOP**

194 The mice were anesthetized with 2.5% isoflurane and 100% oxygen using SomnoSuite. A previously
195 validated commercial rebound tonometer (TonoLab, Colonial Medical Supply) was used to take three
196 sets of six measurements of IOP in each eye. The IOP measurement and recording were carried out in a
197 blinded manner by the experimenter to minimize outcome bias. Right and left eye measurement sets
198 were alternated with the initial eye selected randomly. All measurements were taken between 3 and 5
199 min after isoflurane inhalation based on prior studies. As indicated by the manufacturer, the tonometer
200 was fixed horizontally for all measurements, and the tip of the probe was 2–3 mm from the eye. The
201 probe contacted the eye perpendicularly over the central cornea. The average of a set of measurements
202 was accepted only if the device indicated that there was "no significant variability" (as per the protocol
203 manual; Colonial Medical Supply). Daytime measurements were taken between 11:00 and 15:00 h.
204 Baseline IOP was measured before saline and viral vector injection. After injection, IOP was measured
205 every 10 days until 50 days post-injection.

206 **2.13 Gene expression analysis**

207 Total RNA was extracted from HTM cells using the Trizol method following the manufacturer's protocol.
208 The RNA amounts measurement, cDNA conversion, and qPCR reaction were conducted as published
209 before (54). Sequence-specific forward and reverse oligonucleotide primers for the indicated genes are
210 provided in **Table 2**.

211 q PCR reaction was performed and calculated by the delta-delta Ct method as described earlier (54, 61).
212 The normalization was performed using 18S ribosomal RNA (18S rRNA) for HTM.

213 **TABLE 2:**

SREBP1 Transcript 1 (F1V1)	Forward	CTGACCGACATCGAAGGTGA
	Reverse	AAGTGCAATCCATGGCTCCG
SREBP1 Transcript 2 (F1V2)	Forward	GCTGACCGACATCGAAGACA
	Reverse	CAGGAGGTGGAGACAAGCTG
SREBP1 Transcript 3 (F1V3)	Forward	AACGGCTTCAAAAATCCGCC
	Reverse	CCAGCATAGGGTGGGTCAAA
SREBP2 Transcript 1 (F2V1)	Forward	GGTTGTCGGGTGTCATGGG
	Reverse	TTGCAGCATCTCGTCGATGT
SCAP Transcript 1	Forward	CTGGAGAAGCTGGACTGAGC
	Reverse	CCCAAAGTGCCTGACAGATG
Total-SREBP1	Forward	CAACACAGCAACCAGAAACTC
	Reverse	CTCCACCTCAGTCTTCACG
Total-SREBP2	Forward	ATTCAGCACCACTCCGCAG
	Reverse	GCCCCATCATTACAGGCATTG
LDLR	Forward	TTCACTCCATCTCAAGCATCG
	Reverse	ACTGAAAATGGCTTCGTTGATG
HMGCS1	Forward	TTCCCTTGCATCTGTTCTAGC
	Reverse	TTTTATCAAGAGCAGACCCCG
HMGCR	Forward	ACAGATACTTGGGAATGCAGAG
	Reverse	CTGTCGGCGAATAGATACACC
ACC	Forward	ACAGTGGAGCAAGAATCGG
	Reverse	AATGGACAGAGTTGAGAGCAC
FASN	Forward	AAGCTCTTTCACTTCGGAGG
	Reverse	GGGCATTAACACTTTTGGACG
PPARG	Forward	ATCAAAGTGGAGCCTGCATC
	Reverse	CGACATTCAATTGCCATGAG
ACS	Forward	GGGAAGAGTTGGAAGGTGAAG
	Reverse	GCAGCCATCTCCTGTAACATAG
GPAT	Forward	GTGGAGTGTAGCAAGAGGTG
	Reverse	CAGGGAAAGTAGAGCAGACAC
FN	Forward	GGTGACACTTATGAGCGTCCTAAA
	Reverse	AACATGTAACCACCAGTCTCATGTG
COL1α	Forward	GAGAGCATGACCGATGGATT
	Reverse	CCTTCTTGAGGTTGCCAGTC
COL4α	Forward	TGTGGATCGGCTACTCTTTTG
	Reverse	TAGTAATTGCAGGTCCCACG
	Forward	TCAAGTCCTTCACCAAGCG

COL6α	Reverse	ATCTCCACCTCGTCACTGTA
TNC	Forward	CACTACACAGCCAAGATCCAG
	Reverse	TCGTGTCTCCATTCAGCATTG
TGFβ2	Forward	TTGACGTCTCAGCAATGGAG
	Reverse	TTCGCCTTCTGCTCTTGTTT
SSPN	Forward	AGGTTGACGAACGGACATG
	Reverse	TGTGAGCTGCGAATAGTGG
18S	Forward	CTACCACATCCAAGGAAGCA
	Reverse	TTTTTCGTCACTACCTCCCCG

214

215 **2.14 Protein Analysis by Immunoblotting**

216 For nuclear fraction, cells were collected from a 10 cm plate using fractionation buffer (20 mM HEPES,
217 10 mM KCl, 2 mM MgCl2, 1 mM EDTA, 1 mM EGTA, 1 mM DTT). After using a 1 mL syringe to pass cell
218 suspension through a 27 gauge needle several times, the sample was centrifuged and a pellet that
219 contains nuclei was collected. The pellet was washed, dispersed, and centrifuged again, then the nuclear
220 fraction was collected by TBS with 0.1% SDS.

221 The whole cell lysates containing total protein were prepared using 1X RIPA buffer composed of 50 mM
222 Tris-HCL (PH 7.2), 150 mM NaCl, 1% NP-40, 0.1% SDS, 1 mM EDTA, and 1 mM PMSF with protease and
223 phosphatase inhibitors (#A32961, ThermoFisher Scientific) and then sonicated. Nuclear extraction was
224 collected using 20mM HEPES (pH 7.4), 10mM KCl, 2mM MgCl2, 1mM EDTA, and 1mM EGTA. Media was
225 collected and concentrated using Nanosep® Centrifugal Devices with Omega™ Membrane 10K
226 (#OD010C34, Pall), and add 1X RIPA to collect the media protein.

227 After determining the protein concentration and the immunoblotting process was performed as
228 published earlier (38, 54). Blots were stripped using mild stripping buffer if required to reprobe for the
229 loading control and multiple proteins within the same molecular weight range. The data were
230 normalized to GAPDH, β-actin, LaminB1, or Ponceau S. Semi-quantitative analyses and fold changes
231 were calculated from the band intensities measured using ImageJ software.

232 **2.15 Protein distribution analysis by immunohistochemistry (IHC) and IF**

233 Tissue sections from formalin-fixed, paraffin-embedded human donor whole globes eyes were prepared
234 at Case Western Reserve University, Cleveland, Ohio. Paraffin-embedded porcine TM tissue slides and
235 mice eyeball slides were prepared at the Histology Core, Indiana University, and immunolabeling was
236 performed. IF staining was done on HTM cells grown on 2% gelatin-coated glass coverslip. The
237 methodologies used for IHC and IF has been published from the lab earlier (20, 54).

238 All the slides were observed under a Zeiss LSM 700 confocal microscope, and z-stack images were
239 obtained and processed using Zeiss ZEN image analysis software.

240 **2.16 Quantitative image analysis**

241 ImageJ (version 1.53a) software was used to analyze the SREBPs nuclear fluorescence intensity in IF
242 HTM cell images and SREBPs and ECM proteins in IHC tissue images. Specifically, the
243 immunofluorescence image obtained from the HTM cells and tissue section was converted into an 8-bit
244 image, then the threshold default setup under Adjust was used to convert the image from grayscale into

245 a binary image. Next, the region of interest (ROI) tool was chosen for analysis. In this analysis, the
246 nuclear area in the HTM cells or different ROIs (equal area) in the TM outflow pathway was chosen in an
247 image, and the intensity was measured and compared between the control and fatostatin.

248 **2.17 Quantitative filamentous actin/globular actin (F-actin/G-actin) ratio measurement**

249 The F-actin/G-actin ratio was measured using G-Actin/F-Actin In Vivo Assay Biochem Kit (#BK037,
250 Cytoskeleton, Inc.), following the manufacturer's instructions.

251 **2.18 Lipid content measurement**

252 HTM cells were plated on 100 mm plates. Post-treatment, cells were counted and equal numbers were
253 collected to be frozen at -80°C. Then the phospholipid, cholesterol, and triglyceride from HTM cells were
254 extracted and measured with a phospholipid quantification assay kit (#CS0001, Sigma-Aldrich),
255 cholesterol quantitation kit (#MAK043, Sigma-Aldrich) and triglyceride quantification kit (#MAK266,
256 Sigma-Aldrich) respectively, following manufacturer's instructions.

257 **2.19 Statistical analysis**

258 All data presented were based on greater than three independent observations. The graphs represent
259 the mean ± standard error. All statistical analyses were performed using Prism 9.3.1 (GraphPad). The
260 difference between the two groups was assessed using paired Student's t-test when parametric
261 statistical testing was applicable. When multiple groups were compared, a two-way analysis of variance
262 followed by the Tukey post hoc test was applied. The p-value < 0.05 was considered a statistically
263 significant difference between the test and control samples.

264 **3. Results:**

265 **3.1 Mechanosensing via SREBPs activation in HTM cells aids in increasing the actin-based contractility**

266 In our recent work (38) on HTM cells subjected to mechanical stress, we showed a significant increase in
267 the N-SREBP2 that is involved in cholesterol biogenesis. To better understand the mechanosensing
268 functionality of SREBPs, here we provide empirical evidence by utilizing multiple systems to qualitatively
269 and quantitatively assess the potential changes in SREBPs localization under mechanical stress. Firstly,
270 we performed IF analysis post cyclic mechanical stretch to look at the changes in the localization of
271 SREBPs. After 2 h of stretch (ST), HTM cells showed strong nuclear localization of SREBP1 (top panel
272 second-row third column, green staining) and 2 (bottom panel second-row third column, green staining)
273 (**Figure 1A**). However, there was no significant difference in actin distribution in HTM cells after 2 h ST
274 (top and bottom panel second-row fourth column, red staining) (**Figure 1A**). Further substantial
275 evidence for increased nuclear localization of SREBPs under mechanical stress was obtained from the
276 acute pressure stress model (20, 54, 62). In porcine anterior segments subjected to two times (2x)
277 elevated pressure (30 mmHg) compared to normal pressure (15 mmHg), we found a significant increase
278 in the N-SREBP1 ($n = 4$, $p = 0.04$) and N-SREBP2 ($n = 4$, $p = 0.03$) (**Figure 1B**). Thus, confirming that
279 mechanical stress promoted both SREBP1 and SREBP2 activation by inducing its nuclear translocation.
280 This prompted us to examine the role of SREBPs in the AH drainage outflow pathway and the regulation
281 of IOP. The expression of SREBP isoforms and SCAP transcripts in HTM cells was identified using reverse-
282 transcription polymerase chain reaction (RT-PCR) in primary HTM cell cultures (**Supplementary Figure**
283 **1A**). Additionally, the SREBP isoforms and SCAP protein were found in HTM and PTM cells. We observed

284 pro-SREBP1 and pro-SREBP2 at ~ 125 kDa, N-SREBP1 and N-SREBP2 at ~ 68 kDa, and SCAP at ~ 140 kDa
285 (**Supplementary Figure 1B and 1C**). IF analysis and confocal imaging of SREBP1, 2, and SCAP distribution
286 in HTM cells and the conventional human AH outflow pathway showed their distinct localization. In HTM
287 cells, both SREBP1 and 2 showed cytoplasmic and nuclear distribution (**Supplementary Figure 1D**).
288 Relatively, SREBP1 was located in the more cytoplasmic and perinuclear region around the ER than in
289 the nucleus. On the other hand, SREBP2 showed a more pronounced baseline nuclear localization than
290 cytoplasmic and SCAP showed cytoplasmic distribution (**Supplementary Figure 1D**). In the anterior
291 chamber angle of a normal human eye, the SREBP1, SREBP2, and SCAP immunopositive cells were seen
292 in the TM-JCT region and the endothelial lining of the SC (**Supplementary Figure 1E**). Interestingly,
293 SREBP1 and 2, as well as SCAP showed specific distribution in the TM-JCT region in the anterior chamber
294 angle. Negative control in the presence of secondary antibody alone did not show any staining
295 (**Supplementary Figure 1F**).

296 Since we found increased SREBPs activation under mechanical stress, to provide more functional
297 outcome of SREBPs nuclear localization, we assessed the effects of constitutively activating SREBPs in
298 HTM cells. For this, we expressed Ad5-N-SREBPs in primary HTM cells *in vitro*. In serum-starved HTM
299 cells treated with Ad5-N-SREBPs, Ad5-N-SREBP1a and Ad5-N-SREBP1c significantly increased (n = 4, p =
300 0.01 and n = 4, p = 0.046, respectively) N-SREBP1 transcripts, Ad5-N-SREBP2 significantly increased (n =
301 4, p = 0.01) N-SREBP2 mRNA expression (**Figure 2A**) in comparison to AdMT control. Similarly, N-SREBP1
302 protein expression significantly increased under Ad5-N-SREBP1a (n = 4, p = 0.0001) and Ad5-N-SREBP1c
303 (n = 4, p = 0.03) treatments and N-SREBP2 (n = 4, p = 0.0005) significantly increased under Ad5-N-
304 SREBP2 treatment (**Figure 2B**). Such increases were also confirmed via IF imaging studies. Increased N-
305 SREBP1 distribution (red staining) inside the nucleus (**Figure 2C and 2D**) due to Ad5-N-SREBP1a (second-
306 row third column) and Ad5-N-SREBP1c (third-row third column) compared with AdMT (first-row third
307 column) and increased N-SREBP2 distribution (red staining) inside the nucleus (**Figure 2E and** 2**F**) due to
308 Ad5-N-SREBP2 (second-row third column) compared with AdMT (first-row third column). A striking
309 feature observed in these cells treated with Ad5-N-SREBPs was altered cell shape with increased
310 lamellipodia and filopodial extensions observed with remarkable changes in the actin cytoskeleton
311 (**Supplementary Figure 2A**, denoted by black arrows). To check the effects of constitutive activation of
312 SREBPs on actin polymerization and focal adhesion (FA) formation in HTM, we used phalloidin to stain
313 the filamentous actin (F-actin) in HTM cells along with FA proteins – vinculin and paxillin. In comparison
314 to AdMT (**Figure 2C, 2D, 2E, and 2F**, first-row fifth column), Ad5-N-SREBP1a (**Figure 2C and 2D**, second-
315 row fifth column), Ad5-N-SREBP1c (**Figure 2C and 2D**, third-row fifth column), and Ad5-N-SREBP2 (**Figure**
316 **2E and 2F**, second-row fifth column) increased F-actin distribution inside HTM cells (purple staining in
317 the merged/individually in grayscale) indicating increased actin polymerization. Interestingly, we also
318 observed that under constitutive activation of SREBPs, there was increased lamellipodia and filopodia
319 formation with a strong lamellipodial actin network (**Figure 2C,** 2**D, 2E, and 2F**, denoted by yellow
320 arrows). Increased distribution of vinculin and paxillin in green staining in the merged/individually in
321 grayscale (denoted by white arrows) at the edge of F-actin was observed in Ad5-N-SREBP1a (**Figure 2C**
322 **and 2D**, second-row fourth column), Ad5-N-SREBP1c (**Figure 2C and 2D**, third-row fourth column), and
323 Ad5-N-SREBP2 (**Figure 2E and 2F**, second-row fourth column) indicating increased FA formation,
324 contractility inside the cells, and mechanosensing by HTM cells. Thus, augmentation of nuclear SREBPs
325 in TM cells helps sense mechanical stress by modulating actin polymerization and FA formation.

326 **3.2 Pharmacological inhibition of SREBPs activation lowers IOP by altering the ECM architecture of the**
327 **TM AH outflow pathway in *ex vivo* porcine perfusion cultures**

328 After deriving a linear relationship between mechanical stress, SREBPs activation, and increased actin
329 polymerization, we hypothesized that loss of SREBPs activity can have a significant effect on IOP. The
330 pharmacological inhibition of SREBPs activity was accomplished using fatostatin (56). To test the
331 inhibitory effect of fatostatin on SREBPs activity in TM, the dose-dependency (0.2, 2, 20 µM) of
332 fatostatin on PTM cells was performed. We found that 20 µM fatostatin for 24 h treatment significantly
333 decreased both N-SREBP1 ($n = 4$, $p = 0.02$) and N-SREBP2 ($n = 4$, $p = 0.02$) from the total protein extract
334 (**Supplementary Figure 3A and 3B**). The 20 µM fatostatin did not show cytotoxic effects when tested
335 using FDA and PI staining (**Supplementary Figure 3C**). The 20 µM fatostatin treatment for 24 h in PTM
336 cells showed a significant decrease in N-SREBP1 ($n = 4$, $p = 0.01$) and N-SREBP2 ($n = 4$, $p = 0.02$) protein
337 levels in the nuclear fraction (**Figure 3A**) and same treatment in HTM cells also significantly decreased N-
338 SREBP1 ($n = 4$, $p = 0.03$) and N-SREBP2 ($n = 4$, $p = 0.0001$) protein expression (**Figure 3B**). The SCAP
339 protein expression did not change ($n = 4$, $p = 0.29$) (**Figure 3B**). The IF localization of SREBP1 and SREBP2
340 distribution after fatostatin treatment demonstrated a marked decrease inside of the nucleus compared
341 to the controls (**Figure 3C and D**). Histograms on the right of **Figure 3C and D** represent the ImageJ-
342 based quantification of nuclear SREBPs fluorescence intensities showing a significant decrease in N-
343 SREBP1 ($n = 5$, $p = 0.02$) and N-SREBP2 ($n = 5$, $p = 0.001$) fluorescent staining. Thus, providing the proof-
344 of-concept for fatostatin can inhibit SREBPs activity in TM cells.

345 We then tested the effect of SREBPs inactivation via fatostatin on IOP *ex vivo* using the porcine organ
346 culture system. Perfusion of 20 µM fatostatin significantly decreased IOP by 12 h ($n = 5$, $p = 0.04$), and
347 sustained until 22 h ($n = 5$, $p < 0.05$) (**Figure 3E**). To determine the effects of fatostatin on the TM
348 outflow pathway structures, we analyzed the histological changes. The H and E staining did not show
349 any marked difference in the AH outflow pathway (**Figure 3F**). Confocal imaging of the TM outflow
350 pathway perfused with fatostatin resulted in an appreciable decrease in the immunostaining of SREBP1
351 and SREBP2 (**Figure 3G**). ImageJ-based quantification of fluorescence intensity in the
352 immunofluorescence image showed a significant decrease in SREBP1 staining ($n = 5$, $p = 0.04$) and
353 SREBP2 staining ($n = 5$, $p = 0.04$) (**Figure 3G, right panel**). We provided evidence for changes in the
354 contractile properties of TM cells upon SREBPs activation. On the corollary, we investigated the ECM
355 protein changes upon SREBPs inactivation as the ECM remodeling is affected due to changes in the
356 cellular contractile machinery (63). We found that both COL1A and FN in the TM-JCT region showed a
357 marked decrease compared to the control (**Figure 3H**), which is represented in the histogram for COL1A
358 staining ($n = 5$, $p = 0.0001$), and FN staining ($n = 5$, $p = 0.0001$) in the TM outflow pathway (**Figure 3H,**
359 **right panel**). To get more insights into the quantification of protein levels, we performed
360 immunoblotting with the protein extracted from the TM tissue obtained from DMSO and fatostatin-
361 perfused eyes. In agreement with IHC results, we found that compared to DMSO-perfused porcine TM
362 tissue, fatostatin-perfused porcine TM tissue shows significantly decreased expression of N-SREBP1 ($n =$
363 4, $p = 0.005$), N-SREBP2 ($n = 4$, $p = 0.03$), COL1A ($n = 4$, $p = 0.01$), and FN ($n = 4$, $p = 0.03$) (**Figure 3I**).
364 Thereby, we demonstrate that the direct inhibition of SREBPs activity significantly lowers the IOP by
365 decreasing ECM in the TM outflow pathway.
366
367 **3.3 Molecular inactivation of SREBPs by knocking down SCAP in *SCAP$^{f/f}$* mice lowers IOP *in vivo***

368 We checked the effects of SREBPs inactivation on IOP regulation in *SCAP$^{f/f}$* mice *in vivo*. Conditional
369 knockdown of SCAP was achieved using intravitreal injection of Ad5.CMV.iCre-eGFP in *SCAP$^{f/f}$* mice
370 inducing the loss of SCAP in the TM tissue due to Cre/lox recombination. The cohorts were divided into

371 four groups - three injection groups: Ad5.CMV.iCre-eGFP, Ad5.CMV.eGFP, and saline and one uninjected
372 or the untouched group. Among the injected groups, Ad5.CMV.eGFP injection served as sham virus
373 control and injection of saline served as the sham injection control. The IOP was measured over time in
374 anesthetized *SCAP*$^{f/f}$ mice before injection, and every 10 days after injection until 50 days post-injection.
375 Data presented here show the mean IOP ± SEM in mmHg. The Ad5.CMV.iCre-eGFP injection group
376 displayed a significant IOP lowering (12.97 ± 0.71, n = 10) compared to Ad5.CMV.eGFP injection group
377 (21.74 ± 1.47, n = 9, p = 0.0001), saline injection group (20.5 ± 1.00, n = 10, p = 0.0001), and the
378 untouched group (19.67 ± 0.83, n = 9, p = 0.0001) (**Figure 4A**) 10 days after injection. The IOP decrease
379 in Ad5.CMV.iCre-eGFP injection group compared to the control groups sustained up to 30 days post-
380 injection (n = 10, p < 0.05). At post-injection days 40 and 50, IOP in Ad5.CMV.iCre-eGFP injection group
381 was significantly decreased (n = 10, p < 0.05) compared to saline injection and Ad5.CMV.eGFP injection
382 groups. The IOP was also lower than the untouched group, but not statistically significant (**Figure 4A**).
383 We also compared the IOP changes within each group to their baseline normal IOP (before
384 injection/time point 0 days), and the result shows that there was no significant change in IOP levels in
385 untouched, saline injection, and Ad5.CMV.eGFP injection groups. However, within Ad5.CMV.iCre-eGFP
386 injection group, the IOP was significantly decreased 10 days post-injection and sustained till 50 days
387 post-injection (n = 10, p < 0.05) (**Figure 4B**). Upon analyzing percentage changes in IOP (delta IOP %) in
388 each group at each time point, Ad5.CMV.iCre-eGFP injection group showed a decrease of 40.38%
389 compared to the baseline normal (before injection/time point 0 days) with an average decrease of
390 27.85% (**Figure 4C**). The delta IOP % in the control groups were less than 13% changes of baseline
391 normal IOP. (**Figure 4C**). We evaluated IOP changes after SREBPs knock down in adult and old mice to
392 check if aging in combination with SREBPs knockdown influenced IOP. We found IOP was consistently
393 and significantly decreased in Ad5.CMV.iCre-eGFP group compared to Ad5.CMV.eGFP group (n = 5, p <
394 0.05), and it was also lower than the untouched group and saline injection group in the old and adult
395 cohorts (**Supplementary Figure 4A and 4D, respectively**). In both old and adult cohorts, there was no
396 significant change in IOP levels in all sham control groups, but IOP was significantly decreased 10 days
397 post-injection in Ad5.CMV.iCre-eGFP injection group and sustained till 50 days post-injection (n = 5, p <
398 0.05) (**Supplementary Figure 4B and 4E, respectively**). The IOP in Ad5.CMV.iCre-eGFP injection groups
399 showed a decrease of as much as 42.72 % and 43.14 % of baseline normal IOP in old and adult mice,
400 respectively (**Supplementary Figure 4C and 4F, respectively**). All sham control groups showed less than
401 17 % changes of baseline normal IOP in both old and adult mice (**Supplementary Figure 4C and 4F**). At
402 the end of the longitudinal IOP measurement study, the mice eyes were enucleated and processed for
403 histological and immunohistochemical analysis. The H and E staining showed normal open iridocorneal
404 angles and no marked differences in TM morphology in all the groups (**Figure 4D**). Immunostaining in
405 Ad5.CMV.iCre-eGFP injection group compared to all control groups for - SCAP showed a marked
406 decrease in TM (**Figure 4E, green arrow in the inset**), SREBP1 and SREBP2 showed decreased
407 distribution in the nuclear regions in TM (**Figure 4F and 4G, green arrow in the inset**). This data proves
408 that Ad5.CMV.iCre-eGFP injection selectively knockdown SCAP in TM and further inhibited SREBPs
409 activation in TM consistent with decreased IOP.

410 **3.4 Cholesterol metabolism is greatly affected under SREBP inactivation**

411 Since SREBPs are master regulators of lipid biosynthesis, as a proof-of-concept study, we looked at
412 changes in lipid metabolism in HTM cells under fatostatin treatment. HTM cells treated with 20 µM
413 fatostatin for 24 h significantly decreased SREBPs responsive mRNA expression involved in - 1) genes

414 related to cholesterol biosynthesis: low-density lipoprotein receptor (LDLR) (n = 3, p = 0.05),
415 hydroxymethylglutaryl-CoA synthase 1 (HMGCS1) (n = 3, p = 0.10), 3-Hydroxy-3-Methylglutaryl-CoA
416 Reductase (HMGCR) (n = 3, p = 0.049), SREBP2 (n = 3, p = 0.0008); 2) genes involved in fatty acid
417 biosynthesis: acetyl-CoA carboxylase (ACC) (n = 3, p = 0.0002), fatty acid synthase (FASN) (n = 3, p =
418 0.0055), SREBP1 (n = 3, p = 0.0001), peroxisome proliferator-activated receptor gamma (PPARG) (n = 3, p
419 = 0.01), acetyl-CoA synthetase (n = 3, p = 0.0002); and 3) gene regulating triglyceride and phospholipid
420 biosynthesis: glycerol-3-phosphate acyltransferase (GPAT) (n = 3, p = 0.0017) (**Figure 5A**). We also used
421 immunoblotting to check protein expression levels of FAS, HMGCR, and ACC under control and
422 fatostatin treatment. The immunoblotting results show that fatostatin significantly decreased FAS (n = 4,
423 p = 0.049), HMGCR (n = 4, p = 0.02), and ACC (n = 4, p = 0.049) expression (**Figure 5B**). To further confirm
424 the lipid changes under fatostatin treatment, we treated HTM cells with 20 µM fatostatin for 24 h, and
425 after treatment, we counted the number of cells under each treatment and measured normalized
426 phospholipid/cell, normalized cholesterol/cell, and normalized triglyceride/cell. The results show that
427 phospholipid (n = 4, p = 0.0001) (**Figure 5C**), cholesterol (n = 4, p = 0.04) (**Figure 5D**), and triglyceride (n =
428 4, p = 0.04) (**Figure 5E**) were significantly reduced under fatostatin treatment. Interestingly the
429 magnitude of the phospholipid decrease was the highest (~95%). All these results indicate that SREBPs
430 inactivation using fatostatin can lower the total lipid biosynthesis in HTM cells by decreasing the
431 expression of SREBPs responsive genes.
432

433 **3.5 Induction of actin depolymerization machinery and decreasing ECM-based interactions in TM**
434 **defines the cellular basis of SREBPs inhibition on IOP lowering**

435 Next, we checked if SREBPs inactivation by fatostatin modulated actin and FA proteins. We probed for
436 filamentous actin (F-actin) using phalloidin labeling in HTM cells along with FA proteins – vinculin and
437 paxillin. As seen in **Figures 6A and 6B**, compared to DMSO control, 24 h of 20 µM fatostatin treatment
438 on HTM cells demonstrated a marked decrease in the F-actin stress fibers (green staining in
439 merged/grayscale) and sparse distribution of vinculin and paxillin at the edges of F-actin fibers with
440 greater cytoplasmic accumulation (red staining in the merged/grayscale, indicated by white arrows). To
441 further confirm this result, we extracted F-actin and globular actin (G-actin) from control and fatostatin-
442 treated HTM cells separately and checked the changes in F-actin/G-actin ratio in each condition. **Figure**
443 **6C** shows that fatostatin significantly decreased F-actin/G-actin ratio (n = 4, p = 0.04), implying the
444 decreased actin polymerization under fatostatin treatment. Since we also observed decreased FA
445 formation in IF. We next checked the expression of proteins involved in FA formation, F-actin
446 polymerization, and their stabilization. Fascin is a major F-actin bundling protein and regulates the
447 maintenance and stability of parallel bundles of F-actin in various cell types including TM (64),(20).
448 Immunoblotting showed that fatostatin significantly decreased fascin-1 expression (n = 4, p = 0.03)
449 (**Figure 6D**). We did not see any change in vinculin expression (n = 4, p = 0.61) (**Figure 6D**). Thus
450 suggesting that fatostatin changes vinculin distribution at the edge of F-actin fibers, but not its
451 expression. We found that fatostatin significantly decreased LIM kinase 1 (LIMK1) expression (n = 4, p =
452 0.04) (**Figure 6D**), an actin polymerization and stabilization protein(65). Looking at cofilin, we found no
453 significant change in the levels of total-cofilin (T-cofilin) (n = 4, p = 0.97) and phosphorylated cofilin at
454 serine 3 (P-cofilin) (n = 4, p = 0.05), but the ratio of P-cofilin/T-cofilin was significantly decreased in
455 fatostatin treatment (n = 4, p = 0.01) (**Figure 6E**). Therefore, providing evidence for weakening the
456 LIMK1-cofilin-driven actin polymerization. Moreover, we also found that fatostatin treatment increased
457 total-paxillin (T-paxillin) levels (n = 4, p = 0.07), and significantly decreased its tyrosine 118
458 phosphorylated form (P-paxillin) (n = 4, p = 0.03). The ratio of P-paxillin/T-paxillin was significantly
459 decreased in fatostatin treatment (n = 4, p = 0.01) (**Figure 6F**), indicating decreased cell adhesiveness
460 and cellular contractility.

461 Alterations in actin and focal adhesions can have a direct impact on ECM adhesion (66). Consequently,
462 we evaluated the effect of SREBPs activity on ECM protein expression and distribution in TM, we treated
463 HTM cells with 20 μM fatostatin or vehicle DMSO for 24 h. Interestingly, we found that fatostatin
464 significantly decreased all ECM mRNA expression, including FN (n = 4, p = 0.0001), COL1α (n = 4, p =
465 0.0001), COL6α (n = 4, p = 0.0001), COL4α (n = 4, p = 0.0001), tenascin C (TNC) (n = 4, p = 0.0001),
466 transforming growth factor β2 (TGFβ2) (n = 4, p = 0.0001), and sarcospan (SSPN) (n = 4, p = 0.0001)
467 (**Figure 7A**). Consequently, upon fatostatin treatment, the whole cell lysate (CL) protein expression
468 analysis showed a significant reduction of FN (n = 4, p = 0.01) and COL1A (n = 4, p = 0.001) (**Figure 7B**). In
469 addition, secretory ECM levels in conditioned media (CM) demonstrated a significant decrease in FN (n =
470 4, p = 0.02) and COL1A (n = 4, p = 0.001) expression in the fatostatin treatment compared to the control
471 (**Figure 7C**). These results were confirmed using IF. Under fatostatin treatment, FN (**Figure 7D**) and
472 COL1A (**Figure 7E**) immunostaining were comprehensively decreased. Altogether these data indicate
473 that SREBPs inactivation significantly impacts actin polymerization and FA formation. Additionally lowers
474 the intracellular and secreted ECM levels, as well as their distribution. Thus explaining the contribution
475 of the SREBPs activity on the maintenance of IOP by balancing the actin cytoskeletal and ECM
476 remodeling in the TM outflow pathway.

477 **4. Discussion:**

478 This is the first study to provide the initial evidence and elucidate the effects of SREBPs on lipid
479 metabolism, cell contractility, ECM remodeling in TM, and IOP. In this study, we report that SREBPs and
480 SCAP are highly expressed in the TM-JCT region compared to other components in the ocular anterior
481 segment. We found that mechanical stress on TM including acute elevation of IOP significantly increased
482 SREBPs activation. Augmenting SREBP activation induced contractility indicating a perpetual
483 feedforward signaling from mechanical stress sensing by SREBPs resulting in induction of contractile
484 force in the TM. Conversely inhibiting SREBPs activation using fatostatin *ex vivo* or in the *SCAP$^{f/f}$* mice *in*
485 *vivo* significantly lowered the IOP. We hypothesize that such IOP decrease due to SREBPs inactivation
486 lowers the TM contractility and ECM-based stiffness potentially by downregulating lipogenesis. SREBPs
487 inactivation significantly reduced the expression of their responsive lipid genes and enzymes related to
488 lipogenic pathways in HTM cells. Here, we showed that SREBPs inactivation mitigated actin
489 polymerization and actin bundling by lowering the levels of fascin-1, LIMK1, and phosphorylation of
490 paxillin and cofilin. This study strengthens the correlation between lipid changes and tissue stiffness and
491 reinforces the significance and role of actin-cell adhesive interactions in the regulation of IOP
492 homeostasis. Thus, suggesting that the SREBP-SCAP complex could play an important role in the
493 lipogenesis in the TM tissue.

494 Here, we inactivated the SREBP-SCAP pathway using two different approaches to decipher the role of
495 SREBPs in the regulation of IOP. *Ex vivo* perfusion studies using pharmacological inhibition of SREBPs by
496 fatostatin significantly lowered IOP. A significant IOP lowering was achieved only by 12h, which we
497 believe is due to the low concentration (20 μM) used for perfusion. We also predict that the effect of
498 inhibiting a transcription factor will require a longer time to produce the effect since it will require
499 regulation at the gene expression level first followed by changes in protein/enzyme levels and finally
500 effecting physiological changes. On the other hand, *in vivo* studies in *SCAP$^{f/f}$* mice injected with AdCre
501 confirmed that the molecular inactivation of SREBPs by knocking down SCAP significantly lowered IOP by
502 10 days post-injection. In our recent study, we observed that TM cells under mechanical stress showed
503 increased SREBP2 protein levels (38). The SREBP2 is primarily known to contribute to cholesterol

504 production. Based on the levels of cholesteryl ester levels under mechanical stretch, we hypothesized
505 that cholesterol could be used for rapid membrane remodeling and remaining stored as cholesteryl
506 esters (38). As an extension, here we provide the proof that acute elevation of ocular pressure using *ex*
507 *vivo* porcine anterior segment perfusion cultures induced SREBPs activation in TM. Thereby confirming
508 that SREBPs activation is correlated with mechanical stress on TM. The TM adapts to increased
509 mechanical stress by modifying the actin cytoskeleton and the ECM (38, 62). Upon inducing SREBPs
510 activation, we found that there were increased actin stress fibers indicating a strong connection
511 between SREBPs activation and actin polymerization and an impact on IOP homeostasis. Therefore, we
512 speculated that inhibiting SREBPs activation in TM will modulate IOP. Using both *ex vivo* and *in vivo*
513 studies, we provide strong evidence that attenuating the SREBP-SCAP pathway results in significant IOP
514 lowering. *Ex vivo* evidence indicated a significant loss in the ECM components like collagen and
515 fibronectin in the outflow pathway which concurred in the *in vitro* experiments in HTM cells. *In vitro*
516 analysis provided further proof that the inactivation of SREBPs decreased actin fibers and retraction of
517 FAs to the cytosol with very little found at the edges of the cells. The FAs aid in linking the intracellular
518 cytoskeleton to the extracellular ECM (67). A compromise in vinculin and paxillin localization at the edge
519 of F-actin fibers dictates the dissolution of FAs and decreased cell-ECM connections.

520 It has been characterized that the FA vinculin but not paxillin directly interacts with actin (68, 69).
521 Additional mechanistic evidence in our study confirms that SREBPs inactivation regulates vinculin
522 distribution but not expression confirming the requirement of SREBPs activity in modulating the
523 recruitment of vinculin to the FA. Also, a decrease in paxillin phosphorylation suggests a decreased
524 inside-out signaling towards integrin binding to ECM and recruitment of FA (70, 71). Inside the cells, we
525 identified that loss of SREBPs activation lowered the actin-bundling protein fascin-1 (20, 64, 72). The
526 decreased fascin-1 expression under fatostatin treatment can result in a slower rate of actin
527 polymerization with lesser filopodia formation (73, 74). Within this context, the decreased LIMK1
528 resulting in the loss of phosphorylation of cofilin-1 at serine 3 can induce F-actin destabilization and this
529 can prevent contraction and attenuate hypertension (65, 75). Thus, we propose that the loss of cell
530 adhesive interaction upon SREBPs inactivation is an important mechanism in lowering the IOP.
531 Interestingly, we found that there was a strong negative regulation of most of the ECM gene expression
532 upon fatostatin treatment in HTM cells. Though it is not yet clear why SREBPs does not directly regulate
533 the transcription of ECM genes, we believe this to be a result of negative feedback outside-in signaling
534 towards transcribing ECM genes due to the disengagement of ECM.

535 The major function of SREBPs is to regulate lipogenesis. In line, upon inactivation of the SREBP-SCAP
536 pathway, we found a significant and remarkable decrease in total phospholipids in TM. Additionally,
537 both cholesterol and triglycerides were significantly decreased. The current understanding of the
538 correlation between the regulation of lipid levels in the TM outflow pathway with IOP changes is
539 unclear. Lipids levels are known to be varied in aqueous humor from ocular hypertensives (76) (28, 77)
540 and can participate in the pathogenesis of elevated IOP – the bioactive lysophospholipids (lipid growth
541 factors) (29, 78-81), and cholesterol (30-32). Yet the causality has not been completely attributed to
542 increased lipids on IOP elevation. Based on recent epidemiologic studies, there is an association
543 between cholesterol and glaucoma, although the findings have not been conclusive if hyperlipidemia is a
544 cause or an effect of the disease. Some studies found that hyperlipidemia, especially high cholesterol
545 levels, is significantly associated with an increased risk of glaucoma and increased IOP (31, 32, 82) (83)
546 and others show the opposite (84) (85). Interestingly, even though it is not clear how cholesterol is

547 related to the glaucoma risk, there is mounting evidence showing that HMG-CoA reductase inhibitor
548 statin can decrease POAG risk by mitigating disease progression (35, 86, 87). The proposed mechanism
549 for statins to decrease IOP is by inhibiting the isoprenylation of Rho GTPase thus resulting in decreased
550 actomyosin contractile activity and ECM synthesis/assembly (36, 88-90). All these studies imply that
551 there is an association between lipids, ocular hypertension, and POAG. However, the contributions of
552 lipid metabolism in TM for the regulation of TM biomechanics and IOP are blurred (91). We have
553 recently identified that TM cholesterol plays a significant role in the maintenance of the polymerized
554 state of actin, focal adhesion recruitment, and TM membrane tension (*Unpublished study*). Thus,
555 suggesting a strong role of lipids including cholesterol in regulating TM actin-adhesion complex-ECM
556 modulated via the SREBP-SCAP pathway to efficiently maintain the IOP homeostasis. These findings
557 indicate that SREBPs and their downstream lipid biosynthesis pathways have an essential role in TM
558 functions and contribute significantly to IOP regulation. Moreover, multiple rate-limiting enzymes in
559 lipid biogenic pathways like FAS (49, 92), acetyl-CoA carboxylase(ACC) (93, 94), 3-hydroxy-3-
560 methylglutaryl coenzyme A (HMG-CoA) reductase (HMGCR), and SREBPs are implicated in increasing
561 ECM and fibrosis in various tissue types (95-97). ACC catalyzes the carboxylation of acetyl-CoA into
562 malonyl-CoA. This reaction is the first and the rate-limiting step in the biosynthesis of fatty acids.
563 Significantly, Acetyl-CoA metabolism is implicated in POAG (98). Further investigation on the role of
564 these rate limiting enzymes in TM biomechanics is essential to decode their function in IOP regulation.
565 We predict that induction of SREBPs activation can induce IOP elevation by modifying the contractile
566 properties of the TM, which warrants further studies. Though out of scope for this manuscript, we
567 predict that SREBPs can modulate ECM remodeling via lipid-independent pathways. SREBP1 has been
568 shown to bind to the promoter region of TGFβ (99), a major pro-fibrotic factor. Also, SREBP1 can act as a
569 cell surface retention factor for the TGFβ receptor, TβRI, by preventing its secretion in exosomes or
570 directly changing COL VI transcription (100) (101). Thus, pointing to the idea that SREBPs activation can
571 potentially increase ECM production and deposition and IOP elevation in both lipid-dependent and -
572 independent pathways.

573 **5. Conclusion**

574 In summary, this study presents a novel way of lowering IOP by inactivating SREBPs through decreasing
575 lipogenesis, actin-based tension, and attenuating ECM accumulation in TM. Thus, demonstrating the
576 important role of SREBPs in the regulation of TM contractility and stiffness, and IOP regulation. Further
577 modalities of SREBPs regulating the actin cytoskeleton and ECM in TM will aid in identifying better
578 targets for IOP lowering and glaucoma therapy.

579 **6. Conflict of Interest**

580 The authors declare no conflict of interest. The funders had no role in the design of the study; in the
581 collection, analyses, or interpretation of data; in the writing of the manuscript, or in the decision to
582 publish the results.

583 **7. Funding**

584 This project was supported by the National Institutes of Health/ National Eye Institute (R01EY029320)
585 (PPP), Glick Research Endowment Funds (PPP), Cohen AMD Research Pilot Grant (PPP), RPB
586 Departmental Pilot Grant (PPP), Sigma Xi Grant-in-aid (TW) and grant from Research to Prevent
587 Blindness to IU.

588 **10. Acknowledgments**

589 We would like to acknowledge Dr. Nuria Morral, Dr. Benjamin Perrin, Dr. Gary Landreth, and Dr. Tim
590 Corson from IUSM for their useful discussions on the project.

591 **11. References**

592 1. R. N. Weinreb, P. T. Khaw, Primary open-angle glaucoma. *Lancet* **363**, 1711-1720 (2004).
593 2. W. M. Grant, Clinical tonography. *Trans Am Acad Ophthalmol Otolaryngol* **55**, 774-781 (1951).
594 3. W. M. Grant, Experimental aqueous perfusion in enucleated human eyes. *Arch Ophthalmol* **69**,
595 783-801 (1963).
596 4. N. A. Sharif, Therapeutic Drugs and Devices for Tackling Ocular Hypertension and Glaucoma, and
597 Need for Neuroprotection and Cytoprotective Therapies. *Frontiers in pharmacology* **12**, 729249
598 (2021).
599 5. Y. Shiose, Intraocular pressure: new perspectives. *Surv Ophthalmol* **34**, 413-435 (1990).
600 6. L. Bonomi *et al.*, Prevalence of glaucoma and intraocular pressure distribution in a defined
601 population. The Egna-Neumarkt Study. *Ophthalmology* **105**, 209-215 (1998).
602 7. I. Dielemans *et al.*, Primary open-angle glaucoma, intraocular pressure, and systemic blood
603 pressure in the general elderly population. The Rotterdam Study. *Ophthalmology* **102**, 54-60
604 (1995).
605 8. H. A. Quigley, Open-angle glaucoma. *The New England journal of medicine* **328**, 1097-1106
606 (1993).
607 9. J. B. Saaddine, K. M. Narayan, F. Vinicor, Vision loss: a public health problem? *Ophthalmology*
608 **110**, 253-254 (2003).
609 10. Y. C. Tham *et al.*, Global prevalence of glaucoma and projections of glaucoma burden through
610 2040: a systematic review and meta-analysis. *Ophthalmology* **121**, 2081-2090 (2014).
611 11. H. A. Quigley, A. T. Broman, The number of people with glaucoma worldwide in 2010 and 2020.
612 *British journal of ophthalmology* **90**, 262-267 (2006).
613 12. M. A. Kass *et al.*, The Ocular Hypertension Treatment Study: a randomized trial determines that
614 topical ocular hypotensive medication delays or prevents the onset of primary open-angle
615 glaucoma. *Arch Ophthalmol* **120**, 701-713; discussion 829-730 (2002).
616 13. A. F. Clark, T. Yorio, Ophthalmic drug discovery. *Nat Rev Drug Discov* **2**, 448-459 (2003).
617 14. A. J. Lee, I. Goldberg, Emerging drugs for ocular hypertension. *Expert Opin Emerg Drugs* **16**, 137-
618 161 (2011).
619 15. L. Crawley, S. M. Zamir, M. F. Cordeiro, L. Guo, Clinical options for the reduction of elevated
620 intraocular pressure. *Ophthalmol Eye Dis* **4**, 43-64 (2012).
621 16. D. K. Sunderland, A. Sapra, "Physiology, Aqueous Humor Circulation" in StatPearls. (Treasure
622 Island (FL), 2022).
623 17. W. D. Stamer, The cell and molecular biology of glaucoma: mechanisms in the conventional
624 outflow pathway. *Invest Ophthalmol Vis Sci* **53**, 2470-2472 (2012).
625 18. D. W. Abu-Hassan, T. S. Acott, M. J. Kelley, The Trabecular Meshwork: A Basic Review of Form
626 and Function. *J Ocul Biol* **2** (2014).
627 19. T. Carreon, E. van der Merwe, R. L. Fellman, M. Johnstone, S. K. Bhattacharya, Aqueous outflow -
628 A continuum from trabecular meshwork to episcleral veins. *Prog Retin Eye Res* **57**, 108-133
629 (2017).
630 20. A. Soundararajan, S. A. Ghag, S. S. Vuda, T. Wang, P. P. Pattabiraman, Cathepsin K Regulates
631 Intraocular Pressure by Modulating Extracellular Matrix Remodeling and Actin-Bundling in the
632 Trabecular Meshwork Outflow Pathway. *Cells* **10**, 2864 (2021).

633 21. P. P. Pattabiraman, C. B. Toris, The exit strategy: Pharmacological modulation of extracellular
634 matrix production and deposition for better aqueous humor drainage. *Eur J Pharmacol* **787**, 32-
635 42 (2016).
636 22. P. P. Pattabiraman *et al.*, RhoA GTPase-induced ocular hypertension in a rodent model is
637 associated with increased fibrogenic activity in the trabecular meshwork. *The American journal*
638 *of pathology* **185**, 496-512 (2015).
639 23. K. Wang, A. T. Read, T. Sulchek, C. R. Ethier, Trabecular meshwork stiffness in glaucoma. *Exp Eye*
640 *Res* **158**, 3-12 (2017).
641 24. J. A. Vranka, M. J. Kelley, T. S. Acott, K. E. Keller, Extracellular matrix in the trabecular meshwork:
642 intraocular pressure regulation and dysregulation in glaucoma. *Exp Eye Res* **133**, 112-125 (2015).
643 25. E. R. Tamm, B. M. Braunger, R. Fuchshofer, Intraocular Pressure and the Mechanisms Involved in
644 Resistance of the Aqueous Humor Flow in the Trabecular Meshwork Outflow Pathways. *Prog*
645 *Mol Biol Transl Sci* **134**, 301-314 (2015).
646 26. J. D. Humphrey, E. R. Dufresne, M. A. Schwartz, Mechanotransduction and extracellular matrix
647 homeostasis. *Nature reviews. Molecular cell biology* **15**, 802-812 (2014).
648 27. N. V. Azbukina *et al.*, Targeted Lipidomic Analysis of Aqueous Humor Reveals Signaling Lipid-
649 Mediated Pathways in Primary Open-Angle Glaucoma. *Biology (Basel)* **10**, 658 (2021).
650 28. G. Edwards *et al.*, Endogenous ocular lipids as potential modulators of intraocular pressure. *J*
651 *Cell Mol Med* **24**, 3856-3900 (2020).
652 29. P. V. Rao, Bioactive lysophospholipids: role in regulation of aqueous humor outflow and
653 intraocular pressure in the context of pathobiology and therapy of glaucoma. *J Ocul Pharmacol*
654 *Ther* **30**, 181-190 (2014).
655 30. K. M. Madjedi *et al.*, The Association between Serum Lipids and Intraocular Pressure in 2 Large
656 United Kingdom Cohorts. *Ophthalmology* **129**, 986-996 (2022).
657 31. L. Posch-Pertl *et al.*, Cholesterol and glaucoma: a systematic review and meta-analysis. *Acta*
658 *Ophthalmol* **100**, 148-158 (2022).
659 32. S. Wang, X. Bao, Hyperlipidemia, Blood Lipid Level, and the Risk of Glaucoma: A Meta-Analysis.
660 *Invest Ophthalmol Vis Sci* **60**, 1028-1043 (2019).
661 33. J. H. Kang *et al.*, Association of Statin Use and High Serum Cholesterol Levels With Risk of
662 Primary Open-Angle Glaucoma. *JAMA ophthalmology* **137**, 756-765 (2019).
663 34. M. W. Marcus *et al.*, Cholesterol-lowering drugs and incident open-angle glaucoma: a
664 population-based cohort study. *PloS one* **7**, e29724 (2012).
665 35. J. D. Stein *et al.*, The relationship between statin use and open-angle glaucoma. *Ophthalmology*
666 **119**, 2074-2081 (2012).
667 36. J. Song, P. F. Deng, S. S. Stinnett, D. L. Epstein, P. V. Rao, Effects of cholesterol-lowering statins
668 on the aqueous humor outflow pathway. *Invest Ophthalmol Vis Sci* **46**, 2424-2432 (2005).
669 37. C. L. Von Zee, M. P. Richards, P. Bu, J. I. Perlman, E. B. Stubbs, Jr., Increased RhoA and RhoB
670 protein accumulation in cultured human trabecular meshwork cells by lovastatin. *Invest*
671 *Ophthalmol Vis Sci* **50**, 2816-2823 (2009).
672 38. A. Soundararajan *et al.*, Multiomics analysis reveals the mechanical stress-dependent changes in
673 trabecular meshwork cytoskeletal-extracellular matrix interactions. *Front Cell Dev Biol* **10**,
674 874828 (2022).
675 39. H. Shimano, R. Sato, SREBP-regulated lipid metabolism: convergent physiology - divergent
676 pathophysiology. *Nat Rev Endocrinol* **13**, 710-730 (2017).
677 40. H. Shimano, Sterol regulatory element-binding proteins (SREBPs): transcriptional regulators of
678 lipid synthetic genes. *Prog Lipid Res* **40**, 439-452 (2001).
679 41. D. Eberle, B. Hegarty, P. Bossard, P. Ferre, F. Foufelle, SREBP transcription factors: master
680 regulators of lipid homeostasis. *Biochimie* **86**, 839-848 (2004).

681 42. J. D. Horton, J. L. Goldstein, M. S. Brown, SREBPs: activators of the complete program of
682 cholesterol and fatty acid synthesis in the liver. *J Clin Invest* **109**, 1125-1131 (2002).
683 43. J. L. Goldstein, R. A. DeBose-Boyd, M. S. Brown, Protein sensors for membrane sterols. *Cell* **124**,
684 35-46 (2006).
685 44. D. Dorotea, D. Koya, H. Ha, Recent Insights Into SREBP as a Direct Mediator of Kidney Fibrosis via
686 Lipid-Independent Pathways. *Front Pharmacol* **11**, 265 (2020).
687 45. M. Matsuda *et al.*, SREBP cleavage-activating protein (SCAP) is required for increased lipid
688 synthesis in liver induced by cholesterol deprivation and insulin elevation. *Genes Dev* **15**, 1206-
689 1216 (2001).
690 46. J. Sakai, A. Nohturfft, J. L. Goldstein, M. S. Brown, Cleavage of sterol regulatory element-binding
691 proteins (SREBPs) at site-1 requires interaction with SREBP cleavage-activating protein. Evidence
692 from in vivo competition studies. *J Biol Chem* **273**, 5785-5793 (1998).
693 47. S. Daemen, M. Kutmon, C. T. Evelo, A pathway approach to investigate the function and
694 regulation of SREBPs. *Genes Nutr* **8**, 289-300 (2013).
695 48. R. Bertolio *et al.*, Sterol regulatory element binding protein 1 couples mechanical cues and lipid
696 metabolism. *Nat Commun* **10**, 1326 (2019).
697 49. X. Zhao, J. Y. Y. Kwan, K. Yip, P. P. Liu, F. F. Liu, Targeting metabolic dysregulation for fibrosis
698 therapy. *Nat Rev Drug Discov* **19**, 57-75 (2020).
699 50. G. Proctor *et al.*, Regulation of renal fatty acid and cholesterol metabolism, inflammation, and
700 fibrosis in Akita and OVE26 mice with type 1 diabetes. *Diabetes* **55**, 2502-2509 (2006).
701 51. J. H. Lee *et al.*, SREBP-1a-stimulated lipid synthesis is required for macrophage phagocytosis
702 downstream of TLR4-directed mTORC1. *Proc Natl Acad Sci U S A* **115**, E12228-e12234 (2018).
703 52. G. Sorrentino *et al.*, Metabolic control of YAP and TAZ by the mevalonate pathway. *Nat Cell Biol*
704 **16**, 357-366 (2014).
705 53. K. E. Keller *et al.*, Consensus recommendations for trabecular meshwork cell isolation,
706 characterization and culture. *Exp Eye Res* **171**, 164-173 (2018).
707 54. A. Soundararajan, T. Wang, S. A. Ghag, M. H. Kang, P. P. Pattabiraman, Novel insight into the
708 role of clusterin on intraocular pressure regulation by modifying actin polymerization and
709 extracellular matrix remodeling in the trabecular meshwork. *J Cell Physiol* **237**, 3012-3029
710 (2022).
711 55. X. Cheng, J. Li, D. Guo, SCAP/SREBPs are Central Players in Lipid Metabolism and Novel
712 Metabolic Targets in Cancer Therapy. *Curr Top Med Chem* **18**, 484-493 (2018).
713 56. S. Kamisuki *et al.*, A small molecule that blocks fat synthesis by inhibiting the activation of
714 SREBP. *Chem Biol* **16**, 882-892 (2009).
715 57. S. H. Lee, J. H. Lee, S. S. Im, The cellular function of SCAP in metabolic signaling. *Exp Mol Med* **52**,
716 724-729 (2020).
717 58. L. Jiajia *et al.*, Assessment of Neuronal Viability Using Fluorescein Diacetate-Propidium Iodide
718 Double Staining in Cerebellar Granule Neuron Culture. *J Vis Exp* 10.3791/55442 (2017).
719 59. M. Matsuda *et al.*, SREBP cleavage-activating protein (SCAP) is required for increased lipid
720 synthesis in liver induced by cholesterol deprivation and insulin elevation. *Genes & development*
721 **15**, 1206-1216 (2001).
722 60. Y. Kidani *et al.*, Sterol regulatory element–binding proteins are essential for the metabolic
723 programming of effector T cells and adaptive immunity. *Nature Immunology* **14**, 489-499 (2013).
724 61. K. J. Livak, T. D. Schmittgen, Analysis of relative gene expression data using real-time
725 quantitative PCR and the 2(-Delta Delta C(T)) Method. *Methods* **25**, 402-408 (2001).
726 62. P. P. Pattabiraman, T. Inoue, P. V. Rao, Elevated intraocular pressure induces Rho GTPase
727 mediated contractile signaling in the trabecular meshwork. *Exp Eye Res* **136**, 29-33 (2015).

63. P. P. Pattabiraman, P. V. Rao, Mechanistic basis of Rho GTPase-induced extracellular matrix synthesis in trabecular meshwork cells. *Am J Physiol Cell Physiol* **298**, C749-763 (2010).
64. J. Zanet *et al.*, Fascin promotes filopodia formation independent of its role in actin bundling. *Journal of Cell Biology* **197**, 477-486 (2012).
65. O. Bernard, Lim kinases, regulators of actin dynamics. *Int J Biochem Cell Biol* **39**, 1071-1076 (2007).
66. C. Wu, Focal adhesion: a focal point in current cell biology and molecular medicine. *Cell Adh Migr* **1**, 13-18 (2007).
67. B. Geiger, A. Bershadsky, R. Pankov, K. M. Yamada, Transmembrane crosstalk between the extracellular matrix--cytoskeleton crosstalk. *Nat Rev Mol Cell Biol* **2**, 793-805 (2001).
68. J. D. Humphries *et al.*, Vinculin controls focal adhesion formation by direct interactions with talin and actin. *The Journal of cell biology* **179**, 1043-1057 (2007).
69. M. Reinhard, M. Rüdiger, B. M. Jockusch, U. Walter, VASP interaction with vinculin: a recurring theme of interactions with proline-rich motifs. *FEBS Lett* **399**, 103-107 (1996).
70. S. L. Bellis, J. T. Miller, C. E. Turner, Characterization of tyrosine phosphorylation of paxillin in vitro by focal adhesion kinase. *The Journal of biological chemistry* **270**, 17437-17441 (1995).
71. A. M. López-Colomé, I. Lee-Rivera, R. Benavides-Hidalgo, E. López, Paxillin: a crossroad in pathological cell migration. *J Hematol Oncol* **10**, 50 (2017).
72. L. M. Machesky, A. Li, Fascin: Invasive filopodia promoting metastasis. *Commun Integr Biol* **3**, 263-270 (2010).
73. R. Jaiswal *et al.*, The Formin Daam1 and Fascin Directly Collaborate to Promote Filopodia Formation. *Current Biology* **23**, 1373-1379 (2013).
74. D. Vignjevic *et al.*, Role of fascin in filopodial protrusion. *Journal of Cell Biology* **174**, 863-875 (2006).
75. M. Morales-Quinones *et al.*, LIMK (LIM Kinase) Inhibition Prevents Vasoconstriction- and Hypertension-Induced Arterial Stiffening and Remodeling. *Hypertension* **76**, 393-403 (2020).
76. G. Edwards, K. Aribindi, Y. Guerra, S. K. Bhattacharya, Sphingolipids and ceramides of mouse aqueous humor: Comparative profiles from normotensive and hypertensive DBA/2J mice. *Biochimie* **105**, 99-109 (2014).
77. H. Wang, G. Edwards, C. Garzon, C. Piqueras, S. K. Bhattacharya, Aqueous humor phospholipids of DBA/2J and DBA/2J-Gpnmb(+)/SjJ mice. *Biochimie* **113**, 59-68 (2015).
78. P. S. Mettu *et al.*, Role of lysophospholipid growth factors in the modulation of aqueous humor outflow facility. *Invest Ophthalmol Vis Sci* **45**, 2263-2271 (2004).
79. L. T. Y. Ho *et al.*, Role of the autotaxin-lysophosphatidic acid axis in glaucoma, aqueous humor drainage and fibrogenic activity. *Biochimica et Biophysica Acta (BBA) - Molecular Basis of Disease* **1866**, 165560 (2020).
80. M. Honjo *et al.*, Autotaxin–Lysophosphatidic Acid Pathway in Intraocular Pressure Regulation and Glaucoma Subtypes. *Investigative Ophthalmology & Visual Science* **59**, 693-701 (2018).
81. P. Iyer *et al.*, Autotaxin-lysophosphatidic acid axis is a novel molecular target for lowering intraocular pressure. *PloS one* **7**, e42627 (2012).
82. H. C. Lin, C. W. Chien, C. C. Hu, J. D. Ho, Comparison of comorbid conditions between open-angle glaucoma patients and a control cohort: a case-control study. *Ophthalmology* **117**, 2088-2095 (2010).
83. S. Pavljasević, M. Asćerić, Primary open-angle glaucoma and serum lipids. *Bosn J Basic Med Sci* **9**, 85-88 (2009).
84. P. A. Newman-Casey, N. Talwar, B. Nan, D. C. Musch, J. D. Stein, The relationship between components of metabolic syndrome and open-angle glaucoma. *Ophthalmology* **118**, 1318-1326 (2011).

776 85. W. C. Stewart, C. Sine, S. Sutherland, J. A. Stewart, Total cholesterol and high-density lipoprotein
777 levels as risk factors for increased intraocular pressure. *Am J Ophthalmol* **122**, 575-577 (1996).
778 86. P. McCann, R. E. Hogg, R. Fallis, A. Azuara-Blanco, The Effect of Statins on Intraocular Pressure
779 and on the Incidence and Progression of Glaucoma: A Systematic Review and Meta-Analysis.
780 *Investigative Ophthalmology & Visual Science* **57**, 2729-2748 (2016).
781 87. N. Talwar, D. C. Musch, J. D. Stein, Association of Daily Dosage and Type of Statin Agent With
782 Risk of Open-Angle Glaucoma. *JAMA ophthalmology* **135**, 263-267 (2017).
783 88. X. Y. Song *et al.*, Atorvastatin reduces IOP in ocular hypertension in vivo and suppresses ECM in
784 trabecular meshwork perhaps via FGD4. *Int J Mol Med* **49** (2022).
785 89. L. Cong, S. Fu, J. Zhang, J. Zhao, Y. Zhang, Effects of atorvastatin on porcine aqueous humour
786 outflow and trabecular meshwork cells. *Exp Ther Med* **15**, 210-216 (2018).
787 90. C. L. Von Zee, E. B. Stubbs, Jr., Geranylgeranylation facilitates proteasomal degradation of rho G-
788 proteins in human trabecular meshwork cells. *Invest Ophthalmol Vis Sci* **52**, 1676-1683 (2011).
789 91. M. Lakk *et al.*, Membrane cholesterol regulates TRPV4 function, cytoskeletal expression, and the
790 cellular response to tension. *Journal of lipid research* **62**, 100145-100145 (2021).
791 92. M. Y. Jung *et al.*, Fatty acid synthase is required for profibrotic TGF-beta signaling. *FASEB J* **32**,
792 3803-3815 (2018).
793 93. M. Lee *et al.*, Phosphorylation of Acetyl-CoA Carboxylase by AMPK Reduces Renal Fibrosis and Is
794 Essential for the Anti-Fibrotic Effect of Metformin. *J Am Soc Nephrol* **29**, 2326-2336 (2018).
795 94. J. Bates *et al.*, Acetyl-CoA carboxylase inhibition disrupts metabolic reprogramming during
796 hepatic stellate cell activation. *J Hepatol* **73**, 896-905 (2020).
797 95. S.-N. Lin *et al.*, Development of antifibrotic therapy for stricturing Crohn's disease: lessons from
798 randomized trials in other fibrotic diseases. *Physiological Reviews* **102**, 605-652 (2022).
799 96. M. Martin *et al.*, Role of endothelial cells in pulmonary fibrosis via SREBP2 activation. *JCI Insight*
800 **6** (2021).
801 97. M. Matsumoto *et al.*, Acetyl-CoA carboxylase 1 and 2 inhibition ameliorates steatosis and
802 hepatic fibrosis in a MC4R knockout murine model of nonalcoholic steatohepatitis. *PloS one* **15**,
803 e0228212-e0228212 (2020).
804 98. J. N. C. Bailey *et al.*, Hypothesis-independent pathway analysis implicates GABA and Acetyl-CoA
805 metabolism in primary open-angle glaucoma and normal-pressure glaucoma. *Hum Genet* **133**,
806 1319-1330 (2014).
807 99. L. Uttarwar, B. Gao, A. J. Ingram, J. C. Krepinsky, SREBP-1 activation by glucose mediates TGF-β
808 upregulation in mesangial cells. *Am J Physiol Renal Physiol* **302**, F329-341 (2012).
809 100. A. Ferrari, S. Maretto, D. Girotto, D. Volpin, G. M. Bressan, SREBP contributes to induction of
810 collagen VI transcription by serum starvation. *Biochem Biophys Res Commun* **313**, 600-605
811 (2004).
812 101. R. Van Krieken *et al.*, Sterol Regulatory Element Binding Protein (SREBP)-1 is a novel regulator of
813 the Transforming Growth Factor (TGF)-β receptor I (TβRI) through exosomal secretion. *Cell*
814 *Signal* **29**, 158-167 (2017).

815 **Figure Legends:**

816 **Figure 1: Mechanical stress on trabecular meshwork induces SREBPs activation**

817 (**A**) Localization of SREBPs in HTM cells subjected to cyclic mechanical stretch was checked using
818 immunofluorescence (IF). After 2 h of mechanical stress, HTM cells showed strong nuclear localization of
819 both SREBP1 (top panel second-row third column) and SREBP2 (bottom panel second-row third column).
820 Phalliodin was used to stain the distribution of filamentous actin (F-actin) fiber in the cells. After 2 h of

821 mechanical stress, there was no observable difference in actin distribution inside the HTM cells (top and
822 bottom panel second-row fourth column). The nucleus was stained with DAPI in blue. Images were
823 captured in z-stack in a confocal microscope, and stacks were orthogonally projected. Scale bar 20
824 micron. (**B**) Protein expression of both nuclear form SREBP1 (N-SREBP1) and SREBP2 (N-SREBP2) were
825 significantly increased in TM derived from enucleated porcine anterior segments perfused under the
826 elevated pressure of 30 mmHg for 5 h compared with 15 mmHg. The results were based on semi-
827 quantitative immunoblotting with subsequent densitometric analysis. β-actin was used as a loading
828 control. Values represent the mean ± SEM, where n = 4-5 (biological replicates). *$p < 0.05$ was
829 considered statistically significant. CTL: un-stretched control HTM cells, ST: stretched HTM cells.

830 **Figure 2: Constitutive induction of SREBPs activation modulates actin and focal adhesion dynamics**

831 (**A**) Compared to AdMT, Ad5-N-SREBP1a and Ad5-N-SREBP1c treatment on HTM cells significantly
832 increased N-SREBP1 mRNA expression, and Ad5-N-SREBP2 significantly increased N-SREBP2 mRNA
833 expression in HTM cells. 18S were used as internal controls for qPCR analysis. (**B**) Compared to AdMT,
834 Ad5-N-SREBP1 and Ad5-N-SREBP2 significantly increased N-SREBP1 protein expression, and Ad5-N-
835 SREBP2 significantly increased N-SREBP2 protein expression. The results were based on semi-
836 quantitative immunoblotting with subsequent densitometric analysis. β-actin was used as a loading
837 control. (**C**), (**D**), (**E**), and (**F**) Immunofluorescence (IF) shows the distribution of SREBP1, SREBP2,
838 filamentous actin (F-actin) fibers, vinculin, and paxillin in HTM cells under AdMT and Ad5-N-SREBPs
839 treatments. (**C**) and (**D**) Ad5-N-SREBP1a (second-row third column), and Ad5-N-SREBP1c (third-row third
840 column) induced strong staining of SREBP1 in the nucleus in HTM cells compared to AdMT (first-row
841 third column). Similarly, (**E**) and (**F**) Ad5-N-SREBP2 (second-row third column) induced strong staining of
842 SREBPs in the nucleus in HTM cells compared to AdMT (first-row third column). Compared to AdMT
843 (first-row fifth column), (**C**) and (**D**) Ad5-N-SREBP1a (second-row fifth column) and Ad5-N-SREBP1c
844 (third-row fifth column), and (**E**) and (**F**) Ad5-N-SREBP2 (second-row fifth column) caused the increased
845 distribution of F-actin fibers stained by phalloidin (purple/grayscale) in HTM cells, and induced increased
846 lamellipodia and filopodia formation (indicated by yellow arrows). (**C**) and (**D**) Ad5-N-SREBP1a (second-
847 row fourth column), Ad5-N-SREBP1c (third-row fourth column), and (**E**) and (**F**) Ad5-N-SREBP2 (second-
848 row fourth column) also induced more distribution of vinculin (green/grayscale) and paxillin
849 (green/grayscale) at the edges of F-actin fibers (indicated by white arrows) in HTM cells compared to the
850 AdMT (first-row fourth column). The nucleus was stained with DAPI in blue. Images were captured in z-
851 stack in a confocal microscope, and stacks were orthogonally projected. Scale bar 20 micron. Values
852 represent the mean ± SEM, where n = 4 (biological replicates). *$p < 0.05$ was considered statistically
853 significant.

854 **Figure 3: Pharmacological inhibition of SREBP-SCAP pathway lowers IOP**

855 (**A**) Nuclear fraction from PTM cells after 20 μM fatostatin for 24 h treatment. Immunoblotting result
856 shows that both N-SREBP1 (left panel) and N-SREBP2 (right panel) were significantly decreased. Lamin
857 B1 was used as loading control. (**B**) Primary HTM cells were treated with 20 μM fatostatin for 24 h, and
858 immunoblotting results show that both N-SREBP1 (left panel) and N-SREBP2 (middle panel) were
859 significantly decreased under fatostatin treatment, but SCAP protein expression level was no significant
860 difference in two groups (right panel). GAPDH was used as loading control. (**C**) and (**D**)
861 Immunofluorescence (IF) show the changes of SREBP1 and SREBP2 distribution in HTM cells after 20 μM
862 fatostatin treatment (left panel). In the fatostatin treated HTM cells, less SREBP1 (green staining) and

863 SREBP2 (green staining) were distributed inside the nucleus (second row), compared to DMSO treated
864 control HTM cells (first row). The nucleus was stained with DAPI in blue. Images were captured in z-stack
865 in a confocal microscope, and stacks were orthogonally projected. Scale bar 20 microns. Quantification
866 of immunofluorescence images using ImageJ-based fluorescence intensity measurements show a
867 significant decrease in both nuclear SREBP1 and nuclear SREBP2's mean fluorescence intensity in
868 fatostatin treated HTM cells (right panel). Freshly enucleated porcine eyes were perfused with 20 µM
869 fatostatin or DMSO control after baseline was established with perfusion media containing D-glucose at
870 37 °C. (**E**) Graphical representation of relative fold change in IOP showed a significant decrease post 12 h
871 of fatostatin perfusion (red line) and remained significant until 22 h compared to vehicle DMSO perfused
872 control (blue line). (**F**) Histological examination of the outflow pathway tissues using Hematoxylin and
873 Eosin (H and E) staining showed no gross morphological alterations between fatostatin perfusion
874 compared to the DMSO control. Scale bar 100 micron. (**G**) and (**H**) Immunolocalization of SREBP1,
875 SREBP2, ECM proteins, including COL1A and FN (green staining) in the outflow pathway tissue in DMSO
876 control or fatostatin. In the fatostatin perfused eyes, SREBP1, SREBP2, COL1A, and FN (left panel second
877 column) showed a decreased distribution in the TM-JCT region. TM indicates trabecular meshwork. AP
878 indicates aqueous plexus. Images were captured in z-stack in a confocal microscope, and stacks were
879 orthogonally projected. Scale bar 50 micron. Quantification of immunofluorescence images using
880 ImageJ-based fluorescence intensity measurements showed a significant decrease in the fluorescence
881 intensity of SREBP1, SREBP2, COL1A and FN in the TM outflow pathway (right panel). (**I**) Quantitative
882 analysis of protein expression from 20 µM fatostatin perfused TM tissues showed a significant decrease
883 in N-SREBP1, N-SREBP2, COL1A and FN compared to vehicle DMSO perfused control. Lamin B1 was used
884 as loading control. Values represent the mean ± SEM, where n = 4-5 (biological replicates). *$p < 0.05$ was
885 considered statistically significant.

886 **Figure 4: Molecular inactivation of SREBPs by SCAP knockdown lowers IOP**

887 (**A**) Start from 10 days after saline and viral injection, IOP was significantly decreased in Ad5.CMV.iCre-
888 eGFP injection group compared to untouched group, saline injection group, and Ad5.CMV.eGFP
889 injection group. This significant reduction in IOP in Ad5.CMV.iCre-eGFP injection group was sustained
890 until 30 days post-injection. On 40 days and 50 days post-injection, compared to saline injection group
891 and Ad5.CMV.eGFP injection group, IOP in Ad5.CMV.iCre-eGFP injection group was significantly
892 decreased, it was also lower than untouched group, but not statistically significant. (**B**) IOP changes in
893 each group was analyzed and compared to their baseline normal IOP (before injection/time point 0
894 days), the graphical representation shows that IOP was significantly decreased in Ad5.CMV.iCre-eGFP
895 injection group starting from 10 days after injection and sustained until 50 days post-injection. There
896 were no significant changes in IOP level in other control groups. (**C**) IOP percentage change (Delta IOP)
897 compared to their baseline normal IOP in each group was calculated, graphical representation shows
898 that IOP in Ad5.CMV.iCre-eGFP injection group was decreased as much as 40.38 % of baseline normal
899 (before injection/time point 0 days) with an average decrease of 27.85 %. The IOP in other control
900 groups showed less than 13 % changes of baseline normal IOP. (**D**) Histological examination of the TM
901 using Hematoxylin and Eosin (H and E) staining showed no gross morphological alterations between four
902 groups. Scale bar 100 micron. (**E**), (**F**) and (**G**) Immunolocalization of SCAP, SREBP1 and SREBP2 proteins
903 in TM in four groups. SCAP showed decreased distribution in TM in Ad5.CMV.iCre-eGFP injection group
904 compared to all other shame control groups. SREBP1 and SREBP2 showed decreased distribution in the
905 nuclear regions in TM in Ad5.CMV.iCre-eGFP injection group compared to other shame control groups.

906 TM indicates trabecular meshwork and marked by white color arrow. Images were captured in z-stack in
907 a confocal microscope, and stacks were orthogonally projected. Scale bar 50 micron. Top left corner in
908 each image shows magnification of the framed area showing the nuclear regions in TM and marked by
909 green color arrow. Scale bar 10 micron. Values represent the mean ± SEM, where n = 9-10 (biological
910 replicates). *$p < 0.05$ was considered statistically significant.

911 **Figure 5: Inactivation of SREBPs inhibits lipogenesis in HTM cells**

912 (**A**) Fatostatin treatment significantly decreased SREBPs responsive genes mRNA expression involved in
913 1) cholesterol biosynthesis: low-density lipoprotein receptor (LDLR), hydroxymethylglutaryl-CoA
914 synthase 1 (HMGCS1), 3-hydroxy-3-methylglutaryl-CoA Reductase (HMGCR), SREBP2; 2) fatty acid
915 biosynthesis: acetyl-CoA carboxylase (ACC), fatty acid synthase (FASN), SREBP1, peroxisome proliferator-
916 activated receptor gamma (PPARG), acetyl-CoA synthetase ; 3) triglyceride and phospholipid
917 biosynthesis: glycerol-3-phosphate acyltransferase (GPAT). 18S were used as internal controls for qPCR
918 analysis. (**B**) Immunoblotting show that fatostatin significantly reduced FAS, HMGCR, and ACC protein
919 expression compared to the control. GAPDH was used as loading control. (**C**), (**D**) and (**E**) show that
920 fatostatin significantly reduced total lipid biosynthesis in HTM cells, including normalized
921 phospholipid/cell, normalized cholesterol/cell, and normalized triglyceride/cell. Values represent the
922 mean ± SEM, where n = 4 (biological replicates). *$p < 0.05$ was considered statistically significant.

923 **Figure 6: SREBPs inactivation alters actin polymerization machinery and redistributes focal adhesions**

924 (**A**) and (**B**) Immunofluorescence (IF) show the distribution of filamentous actin (F-actin) fiber, vinculin
925 and paxillin distribution in HTM cells under DMSO and fatostatin treatment. Fatostatin caused reduced
926 distribution of F-actin fiber stained by phalloidin (green/grayscale) in HTM cells (first and third column)
927 compared to the control. Fatostatin treatment also caused less distribution of vinculin (red/grayscale)
928 and paxillin (red/grayscale) at the edges of F-actin fiber, but more cytoplasmic distribution (indicated by
929 white arrows) in HTM cells (first and forth column) compared to the control. The nucleus was stained
930 with DAPI in blue. Images were captured in z-stack in a confocal microscope, and stacks were
931 orthogonally projected. Scale bar 20 micron. (**C**) Globular actin (G-actin) and F-actin were extracted from
932 HTM cells treated with DMSO or fatostatin. Immunoblotting shows that fatostatin significantly
933 decreased F-actin/G-actin ratio in HTM cells compared to the control. (**D**) Immunoblotting shows that
934 fatostatin treatment significantly reduced Fascin-1 and LIMK1 protein expression, but no difference in
935 vinculin expression compared to the control. GAPDH was used as loading control. (**E**) Immunoblotting
936 shows that there was no significant difference in phosphor-cofilin (P-cofilin) and total-cofilin (T-cofilin)
937 protein expression level in DMSO and fatostatin treated HTM cells. Ratio of P-cofilin/T-cofilin was
938 significantly decreased in fatostatin treated HTM cells compared to the control. GAPDH was used as
939 loading control. (**F**) Immunoblotting shows that fatostatin significantly decreased phosphor-paxillin (P-
940 paxillin) protein expression level, increased total-paxillin (T-paxillin) protein expression level, and
941 significantly reduced the ratio of P-paxillin/T-paxillin compared to the control. GAPDH was used as
942 loading control. Values represent the mean ± SEM, where n = 4 (biological replicates). *$p < 0.05$ was
943 considered statistically significant, and ns denotes non-significant.

944 **Figure 7: SREBPs inactivation lowers ECM production, secretion, and alters remodeling**

945 (**A**) Regulation of ECM mRNA expression under fatostatin treatment. Fatostatin treatment significantly
946 decreased mRNA expression in fibronectin (FN), collagen 1α (COL1α), collagen 6α (COL6α), collagen 4α

947 (COL4α), tenascin C (TNC), transforming growth factor β2 (TGFβ2), and sarcospan (SSPN) in HTM cells
948 compared to DMSO treated control HTM cells. (**B**) Immunoblotting for whole cell lysate (CL) shows that
949 fatostatin significantly decreased FN, COL1A protein expression in fatostatin treated HTM cells
950 compared to DMSO treated control HTM cells. GAPDH was used as loading control. (**C**) Immunoblotting
951 for conditioned media (CM) shows that fatostatin significantly decreased FN and COL1A protein
952 expression in fatostatin treated HTM CM compared to DMSO treated control HTM CM. PonceauS was
953 used as loading control. (**D**) and (**E**) Immunofluorescence (IF) show the FN and COL1A expression and
954 distribution in HTM cells after DMSO or fatostatin treatment. Fatostatin reduced FN (green staining) and
955 COL1A (green staining) distribution compared to the control. The nucleus was stained with DAPI in blue.
956 Images were captured in z-stack in a confocal microscope, and stacks were orthogonally projected. Scale
957 bar 20 micron. Values represent the mean ± SEM, where n = 4 (biological replicates). *$p < 0.05$ was
958 considered statistically significant.

959 **Supplementary Figure 1: Expression and distribution of SREBP isoforms and SCAP in TM**

960 (**A**) Expression profile of SREBP isoforms and SCAP in primary human trabecular meshwork (HTM) cells
961 by reverse-transcription polymerase chain reaction (RT-PCR) showing that SREBP1 transcript 2, SREBP2
962 transcript 1, and SCAP were expressed in HTM. (**B**) Protein expression of proform SREBP1 (Pro-SREBP1)
963 and SREBP2 (Pro-SREBP2), and nuclear form SREBP1 (N-SREBP1) and SREBP2 (N-SREBP2), and SCAP in
964 primary HTM cells. GAPDH was used as the loading control. (**C**) Protein expression of Pro-SREBP1 and
965 Pro-SREBP2, N-SREBP1 and N-SREBP2, and SCAP in primary porcine trabecular meshwork (PTM) cells.
966 GAPDH was used as the loading control. (**D**) Immunofluorescence (IF) shows the cytosolic distribution of
967 SREBP1 (green staining), SREBP2 (green staining) and SCAP (green staining) in primary HTM cells. The
968 nucleus was stained with DAPI in blue. Images were captured in z-stack in a confocal microscope, and
969 stacks were orthogonally projected. Scale bar 20 microns. (**E**) Tissue distribution of SREBP1 (green
970 staining) and SREBP2 (green staining) and SCAP (green staining) in the aqueous humor (AH) outflow
971 pathway of a normal human eye specimen by IF. The nucleus was stained with DAPI in blue. Images
972 were captured in z-stack in a confocal microscope, and stacks were orthogonally projected. Scale bar 50
973 microns. (**F**) The negative control for SREBPs and SCAP distribution in AH outflow pathway (in the
974 presence of secondary antibody alone) did not show any significant staining (green panel).

975 **Supplementary Figure 2: HTM cell changes after Ad5-N-SREBPs treatment**

976 HTM cells were treated with either AdMT or Ad5-N-SREBPs for 24 h followed by 48 h serum starvation.
977 (**A**) Bright-field cell culture images were captured by Nikon TS100 Inverted Phase Contrast Microscope.
978 After treatment, Ad5-N-SREBPs treated HTM cells displayed increased lamellipodia and filopodial
979 extension formation (indicated by black arrows), compared to AdMT treatment.

980 **Supplementary Figure 3: Dose-dependent effects of fatostatin on SREBPs activation in PTM cells**

981 (**A**) and (**B**) Dose-dependent treatment of fatostatin on PTM cells to test the optimal concentration of
982 fatostatin on TM cells. Immunoblotting shows 20 µM fatostatin for 24 h treatment significantly
983 decreased both N-SREBP1 and N-SREBP2 expression. GAPDH was used as a loading control. (**C**)
984 Examination of the effects of 20 µM fatostatin on primary PTM cell viability. Cell viability assay in serum-
985 starved PTM cells treated with 20 µM fatostatin for 24 h was performed using fluorometric live/dead
986 staining of FDA-PI staining. The first row represents the control DMSO treatment, and the second row
987 represents 20 µM fatostatin treatment of serum-starved PTM cells. The first, second, and the third

988 columns are bright field image of PTM cells 24 h after treatment, FDA, and PI staining respectively. The
989 green channel shows viable cells that take up FDA and emit green fluorescence, and the red channel
990 shows dead cells, which take up PI and give out red florescence. The graphical representation denotes
991 the mean percentage ratio of FDA/PI, including the viable cells (green bar) and the non-viable cells (red
992 bar) in both control and 20 µM fatostatin treated cells. No significant cell death was observed after 20
993 µM fatostatin for 24 h treatment. Values represent the mean ± SEM, where n = 4 (biological replicates).
994 *p < 0.05 was considered statistically significant.

995 **Supplementary Figure 4: Molecular inactivation of SREBPs by knocking down SCAP in old and adult**
996 ***SCAP$^{f/f}$* mice lowers IOP *in vivo***

997 (**A**) In old *SCAP$^{f/f}$* mice, start from 10 days after saline and viral injection, IOP was consistently and
998 significantly decreased in Ad5.CMV.iCre-eGFP injection group compared to Ad5.CMV.eGFP injection
999 group, and sustained until 50 days post-injection. Compared to untouched and saline injection group,
1000 IOP was also lower in Ad5.CMV.iCre-eGFP injection group, but not consistently statistally significant. (**B**)
1001 In old *SCAP$^{f/f}$* mice, IOP changes in each group was analyzed and compared to their baseline normal IOP
1002 (before injection/time point 0 days), the graphical representation shows that IOP was significantly
1003 decreased in Ad5.CMV.iCre-eGFP injection group starting from 10 days after injection and sustained
1004 until 50 days post-injection. There was no significant changes in IOP level in other control groups. (**C**) In
1005 old *SCAP$^{f/f}$* mice, IOP percentage change (Delta IOP) compared to their baseline normal IOP in each
1006 group was calculated, graphical representation shows that IOP in Ad5.CMV.iCre-eGFP injection group
1007 was decreased as much as 42.72 % of baseline normal (before injection/time point 0 days) with an
1008 average decrease of 27.61 %. The IOP in other control groups showed less than 17 % changes of baseline
1009 normal IOP. (**D**) In adult *SCAP$^{f/f}$* mice, start from 10 days after saline and viral injection, IOP was
1010 consistently and significantly decreased in Ad5.CMV.iCre-eGFP injection group compared to
1011 Ad5.CMV.eGFP injection group, and sustained until 50 days post-injection. Compared to untouched,
1012 saline injection group, IOP was also lower in Ad5.CMV.iCre-eGFP injection group, but not consistently
1013 statistally significant. (**E**) In adult *SCAP$^{f/f}$* mice, IOP was significantly decreased in Ad5.CMV.iCre-eGFP
1014 injection group starting from 10 days after injection and sustained until 50 days post-injection. There
1015 were no significant changes in IOP level in other control groups. (**F**) In adult *SCAP$^{f/f}$* mice, IOP in
1016 Ad5.CMV.iCre-eGFP injection group was decreased as much as 43.14 % of baseline normal (before
1017 injection/time point 0 days) with an average decrease of 28.10 %. The IOP in other control groups
1018 showed less than 17 % changes of baseline normal IOP. Values represent the mean ± SEM, where n = 4-5
1019 (biological replicates). *p < 0.05 was considered statistically significant.

1020

1021

1022 **FIGURE 1**

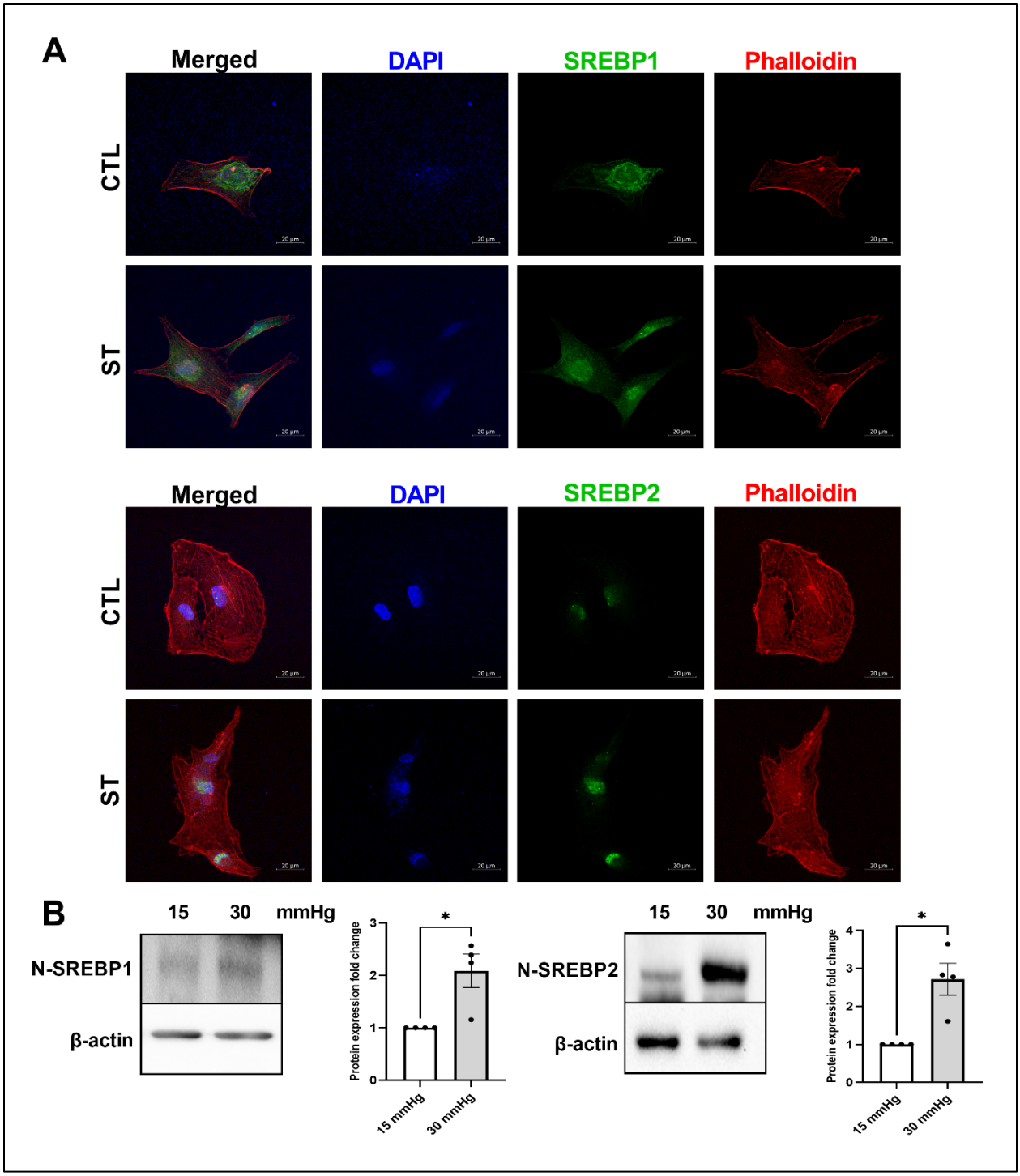

1023

1024

1025

FIGURE 2

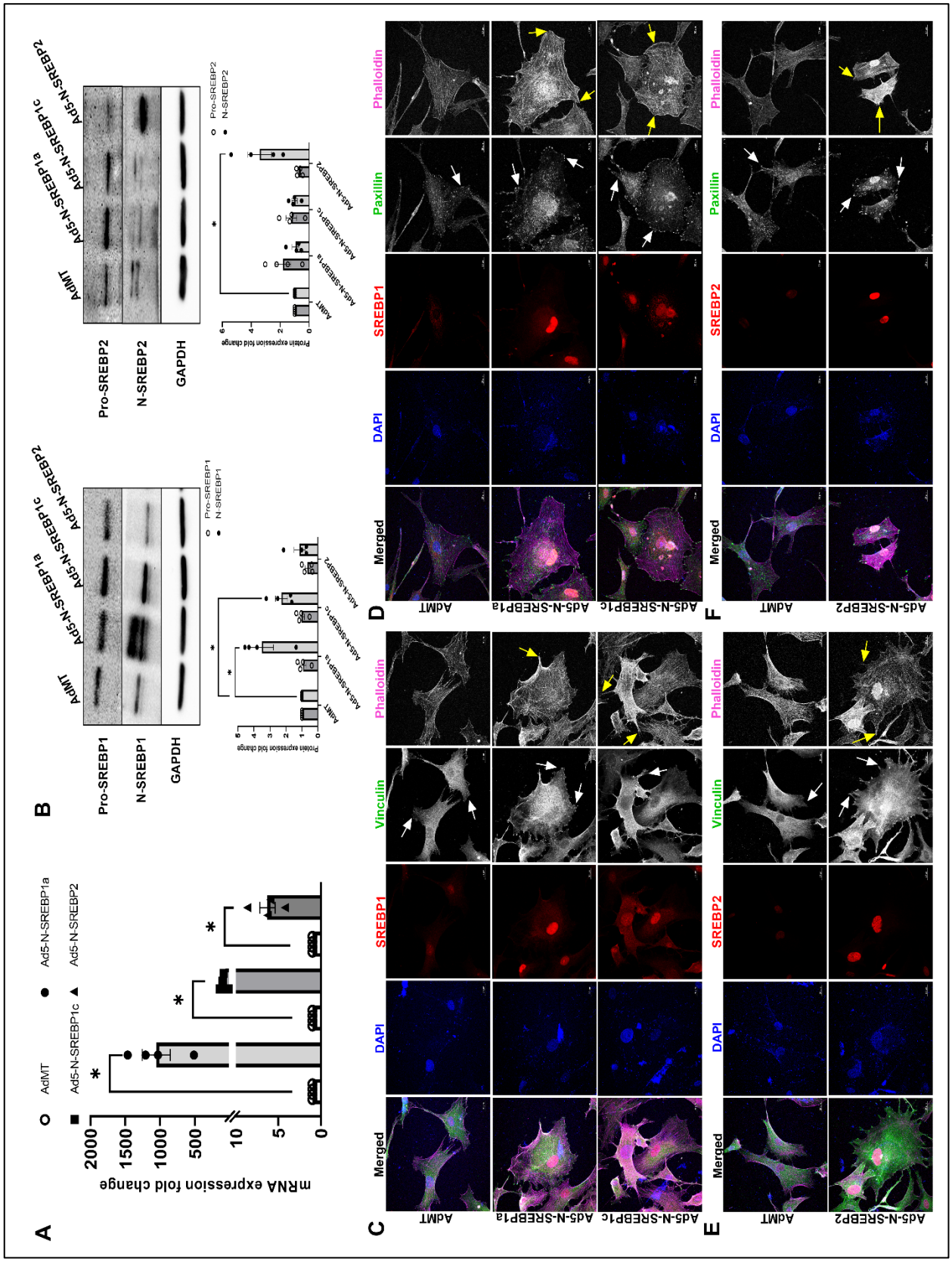
A
mRNA expression fold change
AdMT
Ad5-N-SREBP1c
Ad5-N-SREBP1a
Ad5-N-SREBP2
B
Pro-SREBP1
N-SREBP1
GAPDH
Pro-SREBP2
N-SREBP2
Protein expression fold change
C
D
E
F
Merged
DAPI
SREBP1
SREBP2
Vinculin
Paxillin
Phalloidin

FIGURE 3

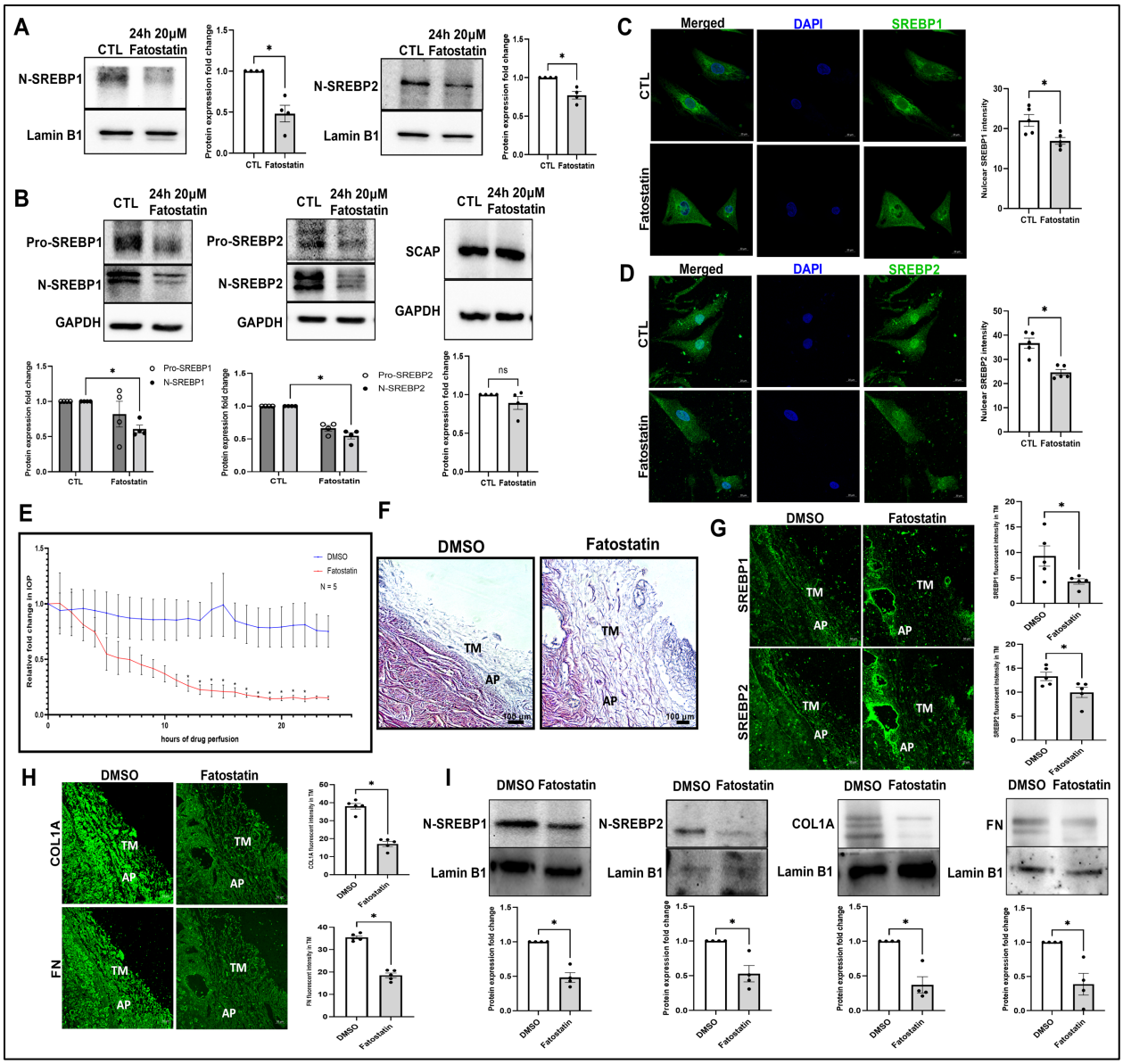
A
24h 20μM
CTL Fatostatin
N-SREBP1
Lamin B1
Protein expression fold change
N-SREBP2
B
Pro-SREBP1
N-SREBP1
GAPDH
Pro-SREBP2
N-SREBP2
SCAP
GAPDH
ns
C
Merged
DAPI
SREBP1
CTL
Fatostatin
Nulcear SREBP1 intensity
D
SREBP2
Nulcear SREBP2 intensity
E
DMSO
Fatostatin
N = 5
Relative fold change in IOP
hours of drug perfusion
F
TM
AP
100 μm
G
SREBP1
SREBP2
H
COL1A
FN
I

1032 **FIGURE 4**

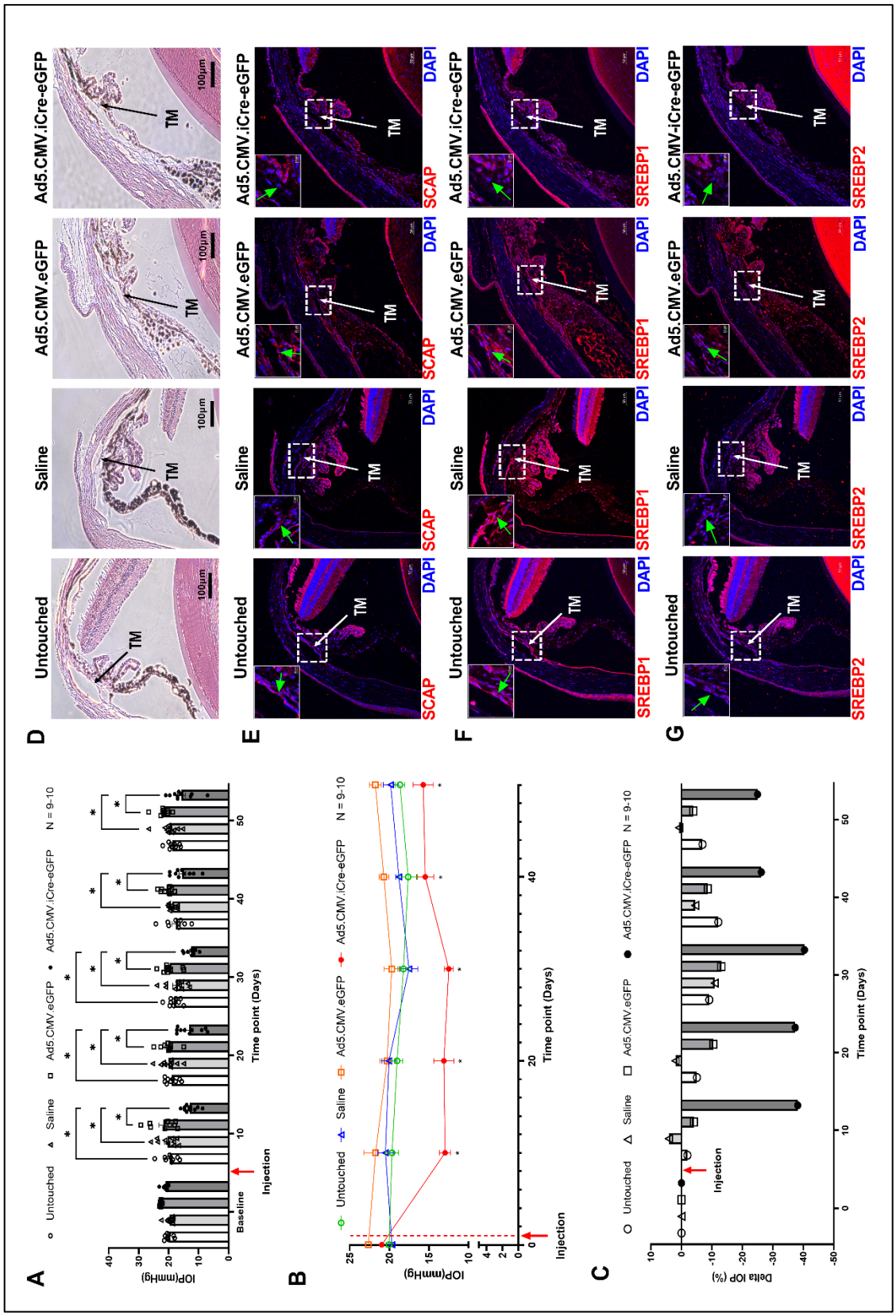

1033

FIGURE 5

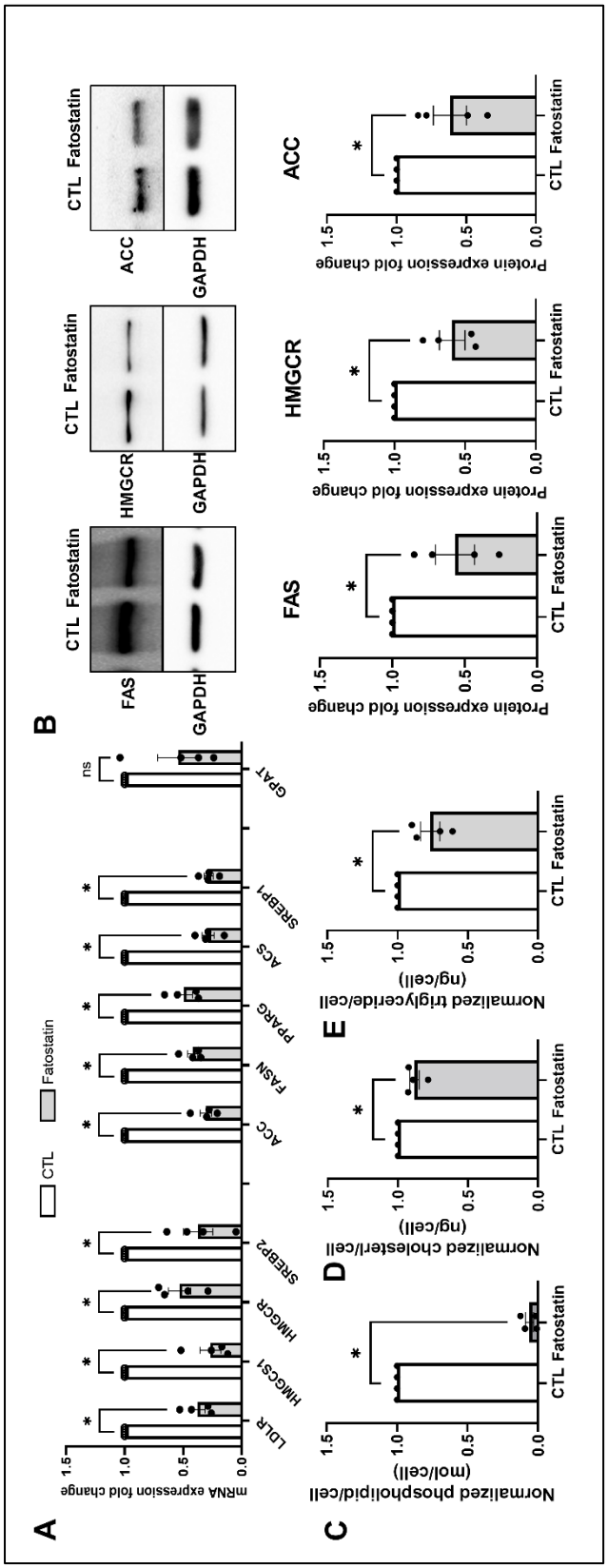
A
CTL
Fatostatin
mRNA expression fold change
1.5
1.0
0.5
0.0
LDLR
HMGCS1
HMGCR
SREBP2
ACC
FASN
PPARG
ACS
SREBP1
GPAT
ns
B
CTL Fatostatin
FAS
GAPDH
HMGCR
ACC
Protein expression fold change
C
Normalized phospholipid/cell
(mol/cell)
D
Normalized cholesterl/cell
(ng/cell)
E
Normalized triglyceride/cell
(ng/cell)

1036 **FIGURE 6**

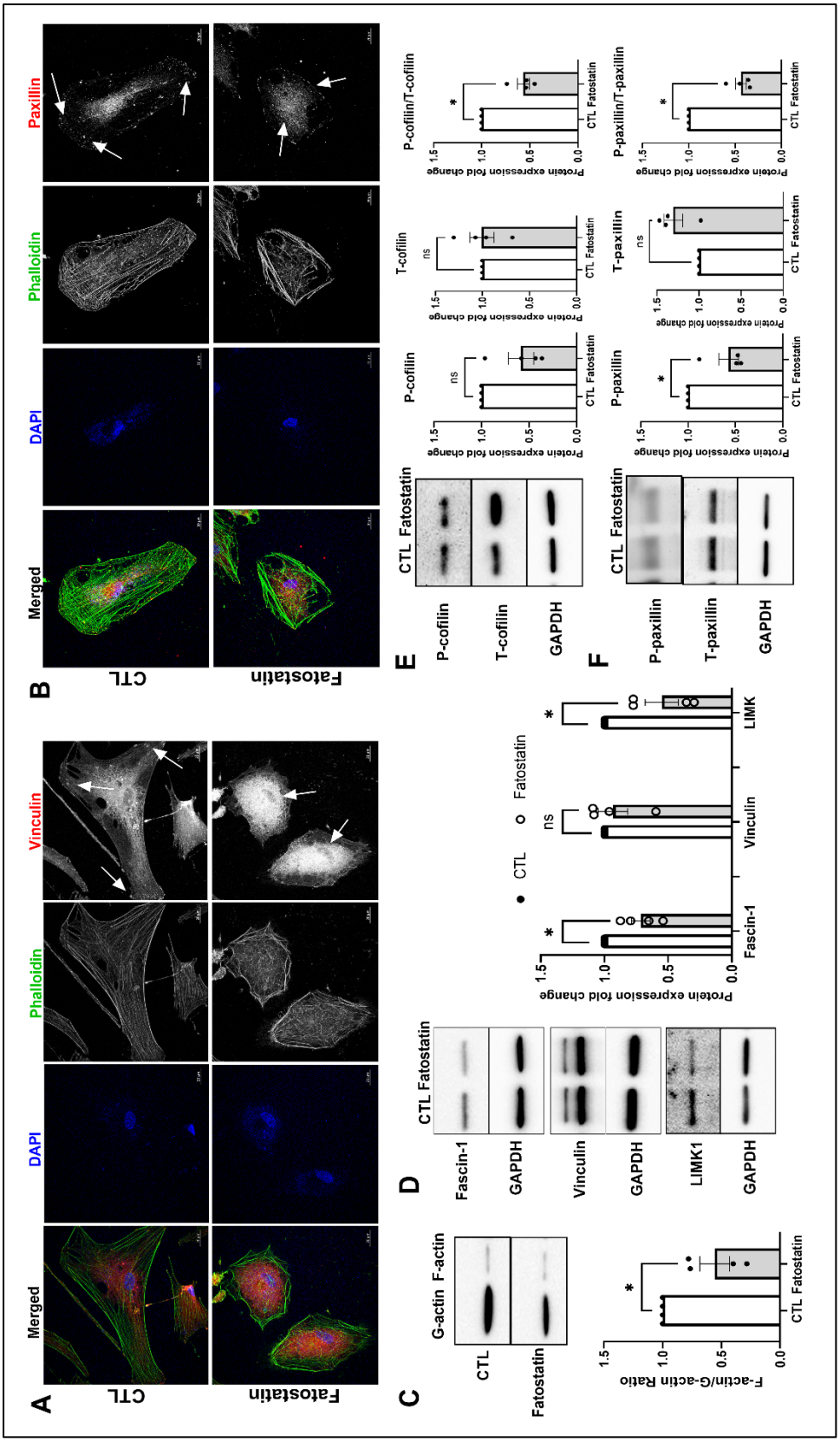

1037

FIGURE 7

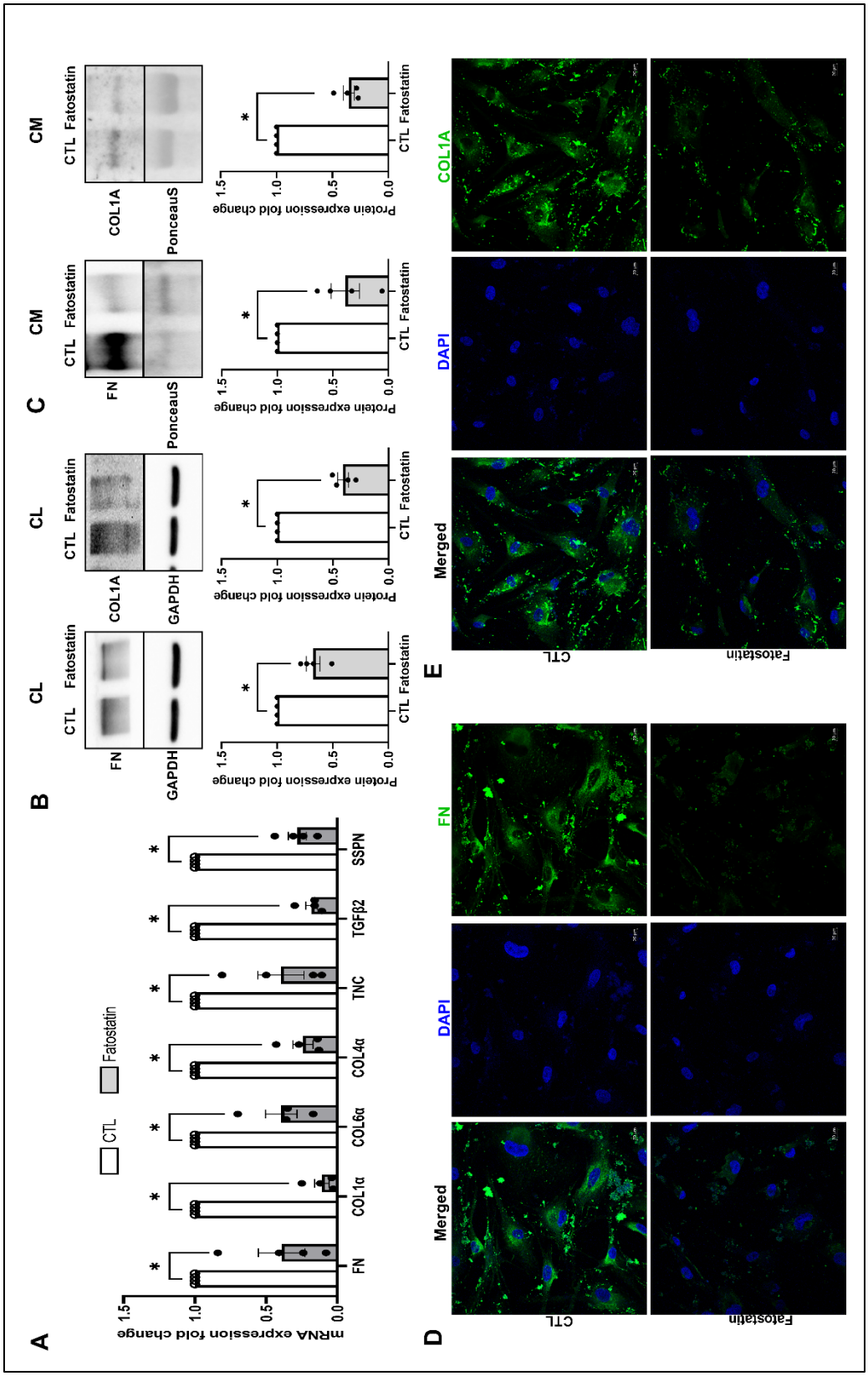
A
mRNA expression fold change
1.5
1.0
0.5
0.0
CTL
Fatostatin
FN
COL1α
COL6α
COL4α
TNC
TGFβ2
SSPN
B
CL
CTL Fatostatin
FN
GAPDH
COL1A
PonceauS
Protein expression fold change
C
CM
CTL Fatostatin
FN
PonceauS
COL1A
D
Merged
DAPI
FN
CTL
Fatostatin
E
Merged
DAPI
COL1A
CTL
Fatostatin

SUPPLEMENTARY MATERIAL:

Supplementary Figure 1:

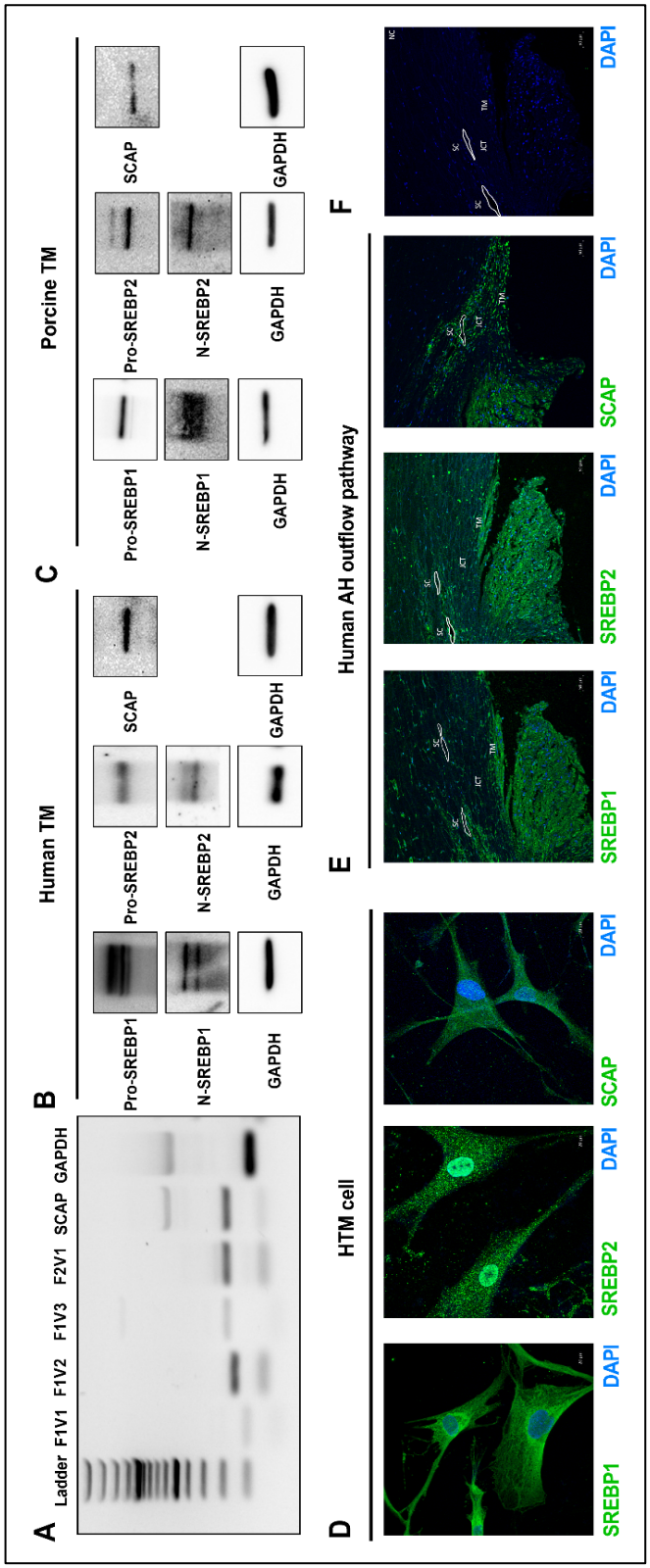

1043 **Supplementary Figure 2:**

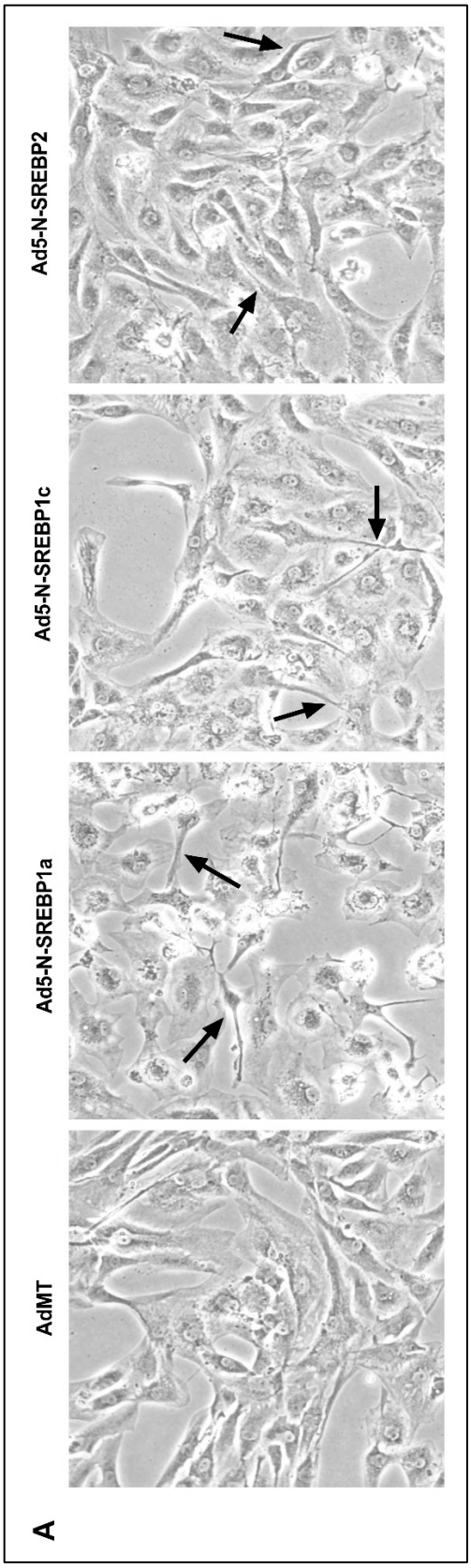

1044

1045 **Supplementary Figure 3:**

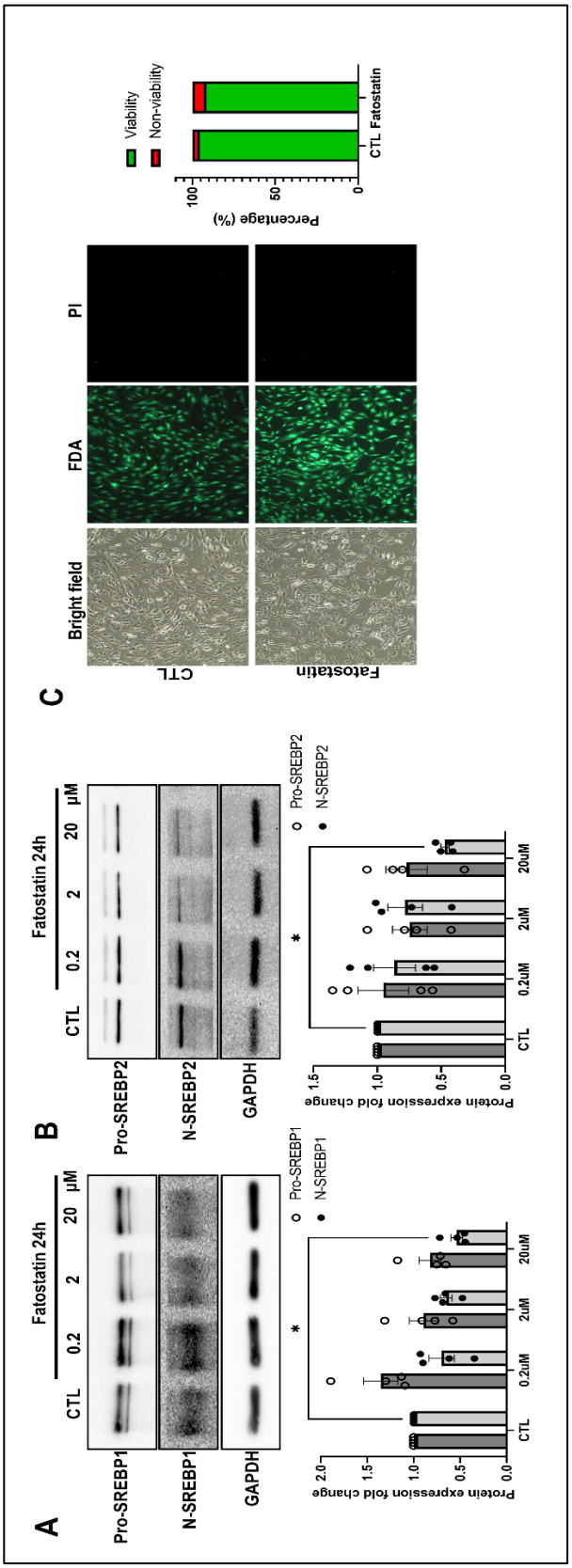

1046

1047 **Supplementary Figure 4:**

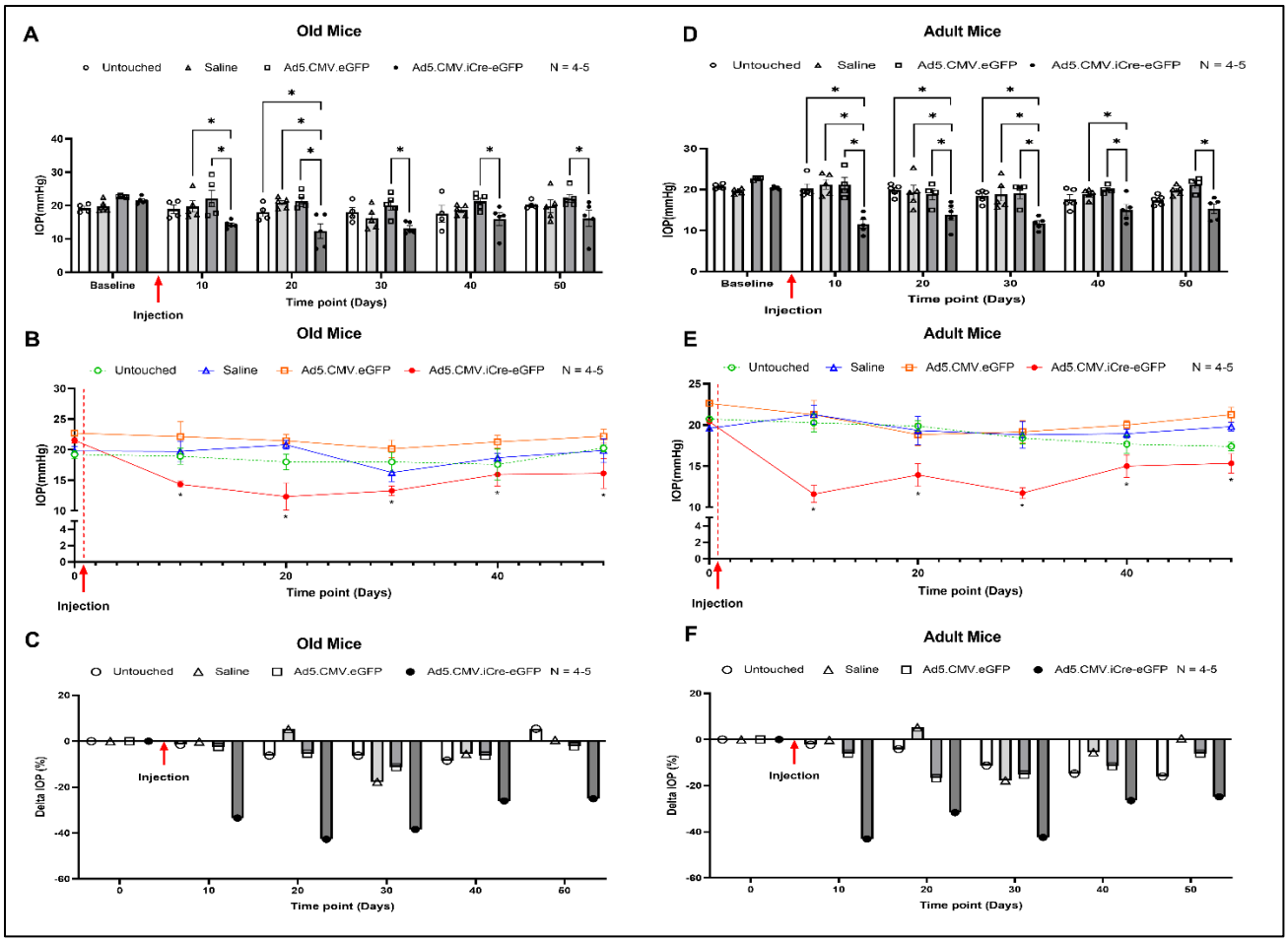

1048

1049

1050

1051